

REPORT DOCUMENTATION PAGE

Form Approved
OMB No. 0704-0188

The public reporting burden for this collection of information is estimated to average 1 hour per response, including the time for reviewing instructions, searching existing data sources, gathering and maintaining the data needed, and completing and reviewing the collection of information. Send comments regarding this burden estimate or any other aspect of this collection of information, including suggestions for reducing the burden, to Department of Defense, Washington Headquarters Services, Directorate for Information Operations and Reports (0704-0188), 1215 Jefferson Davis Highway, Suite 1204, Arlington, VA 22202-4302. Respondents should be aware that notwithstanding any other provision of law, no person shall be subject to any penalty for failing to comply with a collection of information if it does not display a currently valid OMB control number.

PLEASE DO NOT RETURN YOUR FORM TO THE ABOVE ADDRESS.

1. REPORT DATE (DD-MM-YYYY)		2. REPORT TYPE Final Report		3. DATES COVERED (From - To) 15 February 2003 - 31 December 2005	
4. TITLE AND SUBTITLE Adjoint-Based Aeroacoustic Control				5a. CONTRACT NUMBER	
				5b. GRANT NUMBER F49620-03-1-0113	
				5c. PROGRAM ELEMENT NUMBER	
6. AUTHOR(S) Professor Jonathan B. Freund Randall R. Kleinman				5d. PROJECT NUMBER	
				5e. TASK NUMBER	
				5f. WORK UNIT NUMBER	
7. PERFORMING ORGANIZATION NAME(S) AND ADDRESS(ES) Department of Theoretical and Applied Mechanics University of Illinois at Urbana-Champaign Urbana IL 61801				8. PERFORMING ORGANIZATION REPORT NUMBER	
9. SPONSORING/MONITORING AGENCY NAME(S) AND ADDRESS(ES) USAF/AFRL AFOSR 875 North Randolph Street Arlington VA 22203 <i>Dr John Schmusseur</i>				10. SPONSOR/MONITOR'S ACRONYM(S) AFRL-SR-AR-TR-06-0223	
12. DISTRIBUTION/AVAILABILITY STATEMENT Distribution Statement A. Approved for public release; distribution is unlimited.					
13. SUPPLEMENTARY NOTES					
14. ABSTRACT A technique for controlling complex unsteady high-speed flows is being developed. Our approach uses numerical solutions of the adjoint of the compressible flow equations to circumvent the complexity of the flow and directly determine the sensitivity of a specified control objective to changes in actuation. Since this method requires a complete physical description of a turbulent flow which is only currently available from direct numerical simulations, the immediate objective obviously is not to develop a practical control scheme. Instead, the method's utility is in its ability to study flow control in applications like jet noise reduction where a practical prediction capability is lacking. It provides working controls which can be generalized and at the same time provides unique full-fidelity simulation databases of a noisy and its corresponding quieted flow, which can be compared to study the subtle mechanisms of sound generation. The key result of the previous funding period was the development of the adjoint-based formulation in two-dimensions and its (remarkably) successful demonstration on a two-dimensional mixing layer. That was the first time a non-trial-and-error methodology successfully reduced noise from a free shear flow to The summary of our accomplishments of this funding period.					
15. SUBJECT TERMS					
16. SECURITY CLASSIFICATION OF:			17. LIMITATION OF ABSTRACT UU	18. NUMBER OF PAGES 53	19a. NAME OF RESPONSIBLE PERSON
a. REPORT U	b. ABSTRACT U	c. THIS PAGE U			19b. TELEPHONE NUMBER (Include area code)

MAY 22 2006

FINAL REPORT:
ADJOINT-BASED AEROACOUSTIC CONTROL
AFOSR GRANT #F49620-03-1-0113

JONATHAN B. FREUND
RANDALL R. KLEINMAN
MINGJUN WEI

*Department of Theoretical and Applied Mechanics
University of Illinois at Urbana-Champaign
Urbana, IL 61801*

20060710043

DISTRIBUTION STATEMENT A
Approved for Public Release
Distribution Unlimited

Contents

1	Summary	3
2	Introduction	4
3	Two Dimensional Mixing Layer: Summary Of Key Results	6
4	Two-dimensional Mixing Layer: Full Details and Results	9
4.1	Introduction	9
4.2	The two-dimensional mixing layer	11
4.2.1	Flow parameters	11
4.2.2	Governing flow equations	12
4.2.3	Numerical methods	12
4.2.4	Inflow excitation	13
4.2.5	Simulation procedure	14
4.3	Control formulation	14
4.3.1	The control and its objective	14
4.3.2	Sensitivity	15
4.3.3	Adjoint-based optimization: formulation	16
4.3.4	Adjoint-based optimization: numerical implementation	18
4.3.5	Adjoint solution	18
4.3.6	Price term	19
4.4	Results	19
4.4.1	Sound reduction	19
4.4.2	Anti-sound?	21
4.4.3	Spectra	22
4.4.4	The optimized control	25
4.4.5	Control dimensionality	27
4.4.6	Control induced changes to the flow	29
4.5	Discussion and Conclusions	34
5	Three-dimensional Mixing Layer	36
5.1	Numerical Methods	36

5.1.1	Flow parameters and domain	36
5.1.2	Spatial discretization and time advancement	37
5.1.3	Differencing schemes	38
5.1.4	Inflow turbulence procedure	39
5.1.5	Boundary treatments	39
5.1.6	Simulation procedure	41
5.1.7	Three-dimensional adjoint and control considerations	41
5.2	Basic flow results	42
5.2.1	Visualization	42
5.2.2	Mean and turbulence statistics	42
5.3	Preliminary optimization results	44
5.3.1	Cost reduction	45
5.4	Conclusions	46
6	Personnel supported during duration of grant	46
7	AFRL point of contact	46
8	Publications	46
9	Transitions	48
10	Acknowledgment/disclaimer	48
A	Compressible viscous flow equations	48
B	Two-dimensional Adjoint equations	49
C	Three-dimensional Adjoint equations	50
1	Summary	

A technique for controlling complex unsteady high-speed flows was developed. Our approach uses numerical solutions of the adjoint of the compressible flow equations to circumvent the complexity of the flow and directly determine the sensitivity of a specified control objective to changes in actuation. Since this method requires a complete physical description of a turbulent flow, which is only currently available from direct numerical simulations, the immediate objective is not to develop a practical control scheme. Instead, the method's utility is in its ability to study flow control in applications like jet noise reduction where a

practical prediction capability is lacking. It provides working controls which can be generalized and at the same time provides unique full-fidelity simulation databases of a noisy and its corresponding quieted flow, which can be compared to study the subtle mechanisms of sound generation. The key result of the previous funding period was the development of the adjoint-based formulation in two-dimensions and its (remarkably) successful demonstration on a two-dimensional mixing layer. That was the first time a non-trial-and-error methodology successfully reduced noise from a free shear flow to a The summary of our accomplishments of this funding period are:

- We completed a detailed study of different types of control on our mixing layer model of the near-nozzle shear layers of a jet. Different types of flow will be better controlled by different actuations. For jets, fluidic (momentum) type actuators have been demonstrated on full scale engines,¹ but more recently increasing attention is being paid to plasma actuators.² We considered thermal, momentum and mass-source actuators. Within our formulation all worked with comparable effectiveness. For all, it was demonstrated that the noise control results from a genuine change to the flow as a source of sound, not any simple “anti-sound” mechanism.
- We completed a study of the minimal modal degree-of-freedom content of the control identified for them to be effective. This is important for the design of practical actuators.
- Having at the same time a loud and a corresponding quiet controlled flow afforded a unique opportunity to study the mechanisms of the control. It was shown that despite a 10dB reduction of the noise, the flow was superficially unchanged. Its mean flow, turbulence statistics, and apparent large-scale structure were all superficially indistinguishable before and after the application of successful controls. However, decomposition of the flow into empirical eigenfunctions (also Proper Orthogonal Decomposition – POD modes) showed that the control lead to a subtle change in how the large-scale structures advect downstream, which we explained with a simple model of jet noise mechanisms.
- A formulation was derived in three dimensions for the adjoint equations and the entire optimization framework.
- We simulated a turbulent mixing layer with specially designed techniques for setting turbulent inflow conditions. We showed also that this flow has a broad-banded far-field sound spectrum.
- We made an initial demonstration of successful control in three dimensions.

2 Introduction

The ability to diagnose and control highly unsteady turbulent flows is, in many cases, hampered by a lack of accurate models. Noise generation by a turbulent jet is a particularly challenging example, with trial-and-error experimentation being the norm for design improvements despite over 50 years of study. The adjoint-based methods being developed in this project circumvent the present lack of reliable design tools. We build on an existing capability to compute turbulent jet noise from first principles³ and an existing understanding of how to extract useful sensitivity information from adjoint computations in turbulent

flows.⁴ For the first time, a full-physics description of jet noise is available, and is leveraged heavily in this work.

Reduction of jet noise remains an elusive control objective. Certain nozzle geometry modifications are known to reduce noise,⁵ and some of these even have acceptable losses.⁶ Unfortunately, because of the lack of quantitative predictive tools for jet noise, their design always entails some degree of trial-and-error interactions. Thus, it is never known if any sort of optimum has been reached in their design. Presumably, if there were a quick and reliable means of predicting jet noise, control theory could be applied to optimize nozzle geometry with less need for expensive experiments. It would also be easier to investigate active control of jet noise.

It is the nature of jet noise, and aerodynamic sound generation in general, that causes the difficulty. Even for the apparently loud near-sonic jets on civilian aircraft, the noise accounts for only a minuscule fraction of the flow's energy ($\lesssim 10^{-4}$). There is currently not even a phenomenological model for coupling the turbulence to its noise.

In a sense, the radiated acoustic energy comes from individual noise sources that do not quite completely cancel one another, letting only a small amount of energy leak into the far field as sound. In the zero Mach number limit, which has been used successfully in jets, these source are quadrupoles,⁷ so at finite sub-sonic Mach numbers the sources are often said to have a quadrupole character. A related characterization is that individual turbulent structure do not directly radiate because their wavenumber-frequency makeup is such that they can only spawn evanescent pressure waves. It is a subtle aspect of the growth and decay of turbulence structures, or their mutual interactions, that puts energy in components with radiation capable phase velocities. In light of this, it is not surprising that expressions relating near-field turbulence statistics to acoustic radiation are complicated and have not lead to a completely satisfactory prediction capability.

Faced with the complexity of the aeroacoustics of free shear flows, jet noise in particular, we have developed and applied an optimal control methodology. Since trial-and-error experiments have shown modest reduction in noise, we want to determine what the upper limit of this reduction might be: How quiet can a flow be made given a particular set of physical constraints? We focus on active controls since their generality should make them more effective than passive controls. Another question concerns the relative effectiveness of different types of actuation. Any actuation is a combination of mass, momentum, and energy sources. Of these, it is not clear what type or types of actuations will be most effective for noise reduction. Of course, practical considerations will need to be included for any actual actuator design but the relative effectiveness of different types of actuation should also be accounted for, which is not currently possible because it is unknown.

Once a flow has been quieted, as it can be with the algorithm we developed, two further questions arise. The first concerns whether or not the noise reduction can be accomplished by small perturbations so the control would be energy efficient. The second question simply asks what changed? That is, can an effective control mechanism be deduced by comparing the flow before and after it is controlled? To answer these questions, we need a method that circumvents the complexity of the processes and automatically identifies effective controls. We note, however, that since we are primarily interested in studying the mechanics of sound generation, we are not yet concerned with the practical aspects of hardware implementation, though practical constraints can be designed into our methods.

3 Two Dimensional Mixing Layer: Summary Of Key Results

Models based on the large structures in a turbulent jet flow have a long history for jet noise. It is well known that these structures share qualitative, and in some ways quantitative, characteristics with the linear instabilities modes of slowly spreading free shear flows. This similarity has inspired numerous efforts to model jet noise generation, or at least certain aspects of it, with wave-packet sources. These are commonly linear instability modes but relatively *ad hoc* wave packets have also been used with some success.^{8–14} In all these cases the wave-packet models predict certain aspects of the observed radiated noise, but also typically fail in some regard. They might predict the functional form of the directivity, for example, without matching the measured coefficients,⁸ or they might predict silent angles in the directivity, which are not observed.^{8,12}

One particularly troubling aspect of this approach is that the radiated noise can be tremendously sensitive to the subtle details of the wave packet. Consider figure 1 from Freund,¹⁵ which demonstrates that imperceptible changes to a one-dimensional wave-packet noise source can cause order-of-magnitude changes to the noise. Other changes can alter the directivity and so on. A notably quantitative success of wave packets is the successful application of the Crighton & Huerre¹⁰ wave-packet by Colonius *et al.*¹⁶ to a very accurate direct numerical simulation of a harmonically excited two-dimensional mixing layer. Presumably, it is the very regular character of this particular flow—instantaneously it has a seemingly perfect single-streamwise-wavenumber wave-packet form—that facilitates the quantitative agreement. In a turbulent flow, even though there is probably a linear instability mechanism underlying the turbulence, the details of the turbulence would alter any underlying wave-packets sufficiently to affect its noise, disrupting cancellations and making it louder. This disruption is thus inherently coupled to difficult-to-predict features of the flow turbulence and is therefore challenging to model quantitatively.

If this perturbed wave-packet picture of jet turbulence is believed, then we can speculate that a standard free-shear-flow might be in some sense close to a much quieter, more regular wave-packet ‘state’. The question is: Can the correct small perturbations make a nonlinearly active free shear flow (crudely analogous to figures 1 b and d) slightly more regular and thereby much quieter (as in figures 1 a and c)? The principle problem in assessing this possibility is finding the substantially quieter state constrained by the complex nonlinear dynamics of a free shear flow, assuming that such a state exists at all. To do this we formulated the adjoint of the perturbed and linearized compressible flow equations in such a way that its solution, when it is forced by an appropriate metric of the noise, provides the sensitivity of the radiated sound to changes in control actuation. The full details of the formulation are provided elsewhere.¹⁷ With this sensitivity, it is a straightforward but computationally intense task to optimize the actuation to find the perturbation we seek. Since the adjoint formulation is built upon a linearization, the optimization of the nonlinear flow-noise system must be undertaken iteratively.

Because of the expense of the computation and the number of iterations needed, we focus our current effort on a two-dimensional mixing layer, which serves as a model for the near-nozzle region of a jet. The free stream Mach numbers are 0.2 and 0.9. The target for control is $\iint \bar{p}'\bar{p}' dsdt$ on a line Ω extending the length of the computational domain as seen in figure 2. At the inflow of the computation, the flow was exited with 8 randomly selected frequencies between 0 and $2f_o$, where f_o is the linear instability prediction for the locally

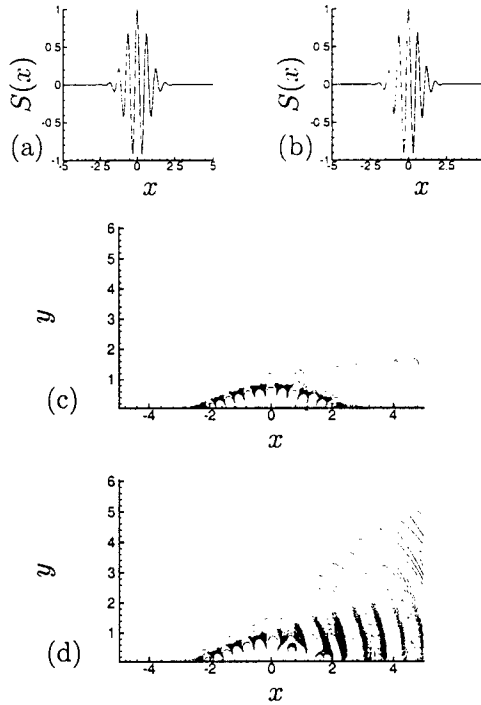


Figure 1: Demonstration of wave packet sensitivity to small perturbations. We assume a one-dimensional source $S(x)$ in a three-dimensional homogeneous medium⁹ whose sound is computed via $p_{tt} + a^2 \Delta p = S(x)\delta(y)$. Shown are (a) an unperturbed source with $S(x) = e^{-\sigma x^2} \cos(\omega t - kx)$ with radiated sound (c); and (b) $S(x) = e^{-\sigma x^2} \cos(\omega t - \kappa(x)x)$, where $\kappa(x) = k + 0.05 \tanh(x)$, and its radiated sound (d). The radiation increases by roughly a factor of ten with this perturbation that is barely visible in (b). Contour levels in (c) and (d) are the same and $\omega/k = 0.5a$, as appropriate for a near-sonic jet.

most amplified instability mode. For contrast, we also simulated and attempted to control the same flow excited by $2f_o$, f_o and 6 sub-harmonics, which is similar to the definitively wave-packet flow studied by Colonius *et al.*¹⁶ In this case, we expect regular vortex roll-ups and pairings and sources much closer to the idealized traveling waves discussed above.

Though our formulation can optimize a broad class of controls, to meet our current objectives we seek the most general control possible and optimize a smooth forcing function with compact support in \mathcal{C} (see figure 2). Each point of its discrete representation is treated as an independent control parameter. The control is remarkably successful, reducing the noise by up to 11dB, which it does with very little energy input,¹⁷ requiring less than 0.01% of the fluctuation kinetic energy in the shear layers. Direct numerical tests confirm that the mechanism of the control is a change to the flow as a source of sound and not so-called anti-sound acoustic cancellations. Optimizing an actual anti-sound source is found to be marginally successful but only on Ω in figure 2. The flow control is successful both on Ω and beyond it and even in the opposite direction in the high-speed stream.

Despite the dramatic noise reduction effected by the control, the flow itself is remarkably unchanged. The mean-flow spreading rates, near-field spectra, second-order fluctuation statistics, and flow visualizations (*e.g.* figure 3) all show only minor changes to the flow before and after the control is applied. This confirms our notion that a random nonlinearly active flow can be perturbed slightly to a close-by quiet state, just as the wave-packet

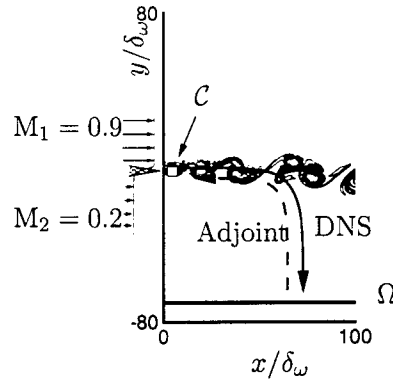


Figure 2: Mixing layer control schematic.

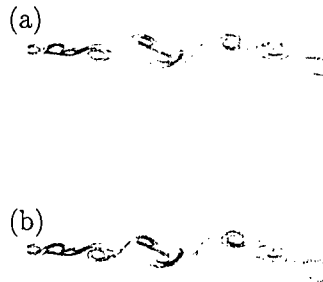


Figure 3: Vorticity visualization of the flow before (a) and after (b) control. The control reduces the noise by over 10dB in this case.

models discussed above would suggest. In contrast, the noise of the harmonically excited flow, which presumably is already in a quiet condition given its regular character, is reduced by less than 0.7dB by the same control scheme. Interestingly, its noise level matches closely that of the controlled randomly excited flow.¹⁷

Despite the superficial similarity of the before and after pictures and fluctuation statistic, the final question we wish to address is whether a more regular underlying wave-packet-like order can be deduced in the controlled flow. This is important for confirming that the wave models whose properties motivated this discussion have some merit in qualitatively describing the mechanism of the control. We investigate this by decomposing the flow into empirical eigenfunctions (POD modes), which we use as surrogates for Fourier modes in the inhomogeneous streamwise direction. Quiet wave-packet sources are expected to have a form with predominantly smooth downstream advection at a subsonic speed. We anticipate forms such as $a_1(t) \cos kx + a_2(t) \sin kx$ multiplied by some slowly varying envelope function. For smooth advection, the coefficients a_1 and a_2 would trace circular paths in their phase plane. This behavior is, of course, observed in the harmonically excited flow.

Figure 4 shows the two most energetic empirical eigenmodes based on a p' L_2 -norm. Comparing the before (figure 4 a) and after (figure 4 b) cases we see that the energy has organized

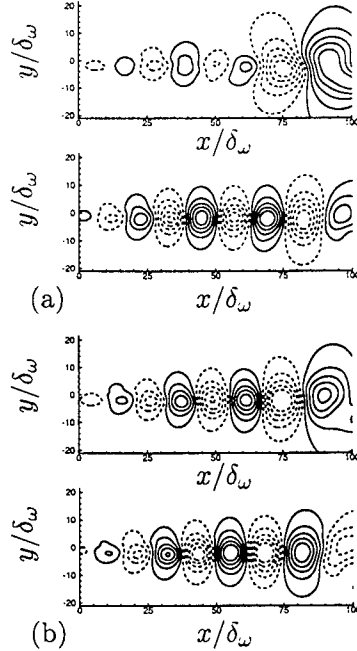


Figure 4: The two most energetic empirical eigenfunction (POD) modes for the pressure field: (a) before and (b) after control.

itself into modes that do indeed fit together much like sines and cosines and would therefore be capable of advecting the structures smoothly downstream. The a_i coefficients of these modes, which reconstruct the flow pressure as

$$p(\mathbf{x}, t) = \sum_{i=1}^N a_i(t) \phi_i(\mathbf{x}), \quad (1)$$

where ϕ_i is the i -th pressure eigenfunction, do indeed now trace a more circular trajectory in the a_1 – a_2 phase plane, as seen in figure 5. Eigenfunctions for other flow variable constructed with a kinetic energy norm show similar behavior.¹⁷ It is also noted elsewhere¹⁷ that the control leads to nearly silent angles at particular radiated frequencies, which are also predicted by some wave-packet models.^{8,12}

We conclude that there has indeed been a subtle ordering induced by the control, which seems to exploit the strong sensitivity of the noise to subtle changes in the form of the source as anticipated by the wave-packet models. Our nonlinearly active randomly excited mixing layer is perturbed only slightly into a nearby much quieter state. Whether or not this picture holds for a three-dimensional turbulent flow is the subject of on-going investigations.

4 Two-dimensional Mixing Layer: Full Details and Results

4.1 Introduction

The generation of sound by a subsonic jet has resisted any simple mechanistic description. While manipulations of the flow equations can provide a hierarchy of theoretical noise-source definitions,¹⁸ the details of the process are masked in the complexity of the flow

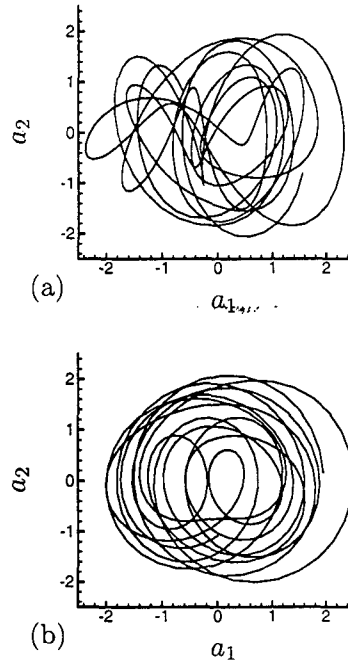


Figure 5: The phase map of coefficients of the most energetic empirical eigenfunction modes of the pressure field: (a) before control; (b) after control.

turbulence. Even then there is the additional complication that most of the turbulence energy does not directly couple to the sound field: it is the subtle growth and decay of the energetic turbulence structures and their interactions that puts energy into radiation-capable noise-source components,^{19,20} however they are defined within a particular model. For example, in the simplest model,⁷ where propagation is by the stationary-medium scalar wave equation, a mode must have a supersonic phase velocity to radiate. This condition is satisfied by only a small portion of the fluctuation energy in a subsonic jet. Statistical descriptions of theoretical noise sources are complex, and models for them currently lack the fidelity for reliable predictive acoustic modeling of general flows. Even direct numerical simulations,^{3,16} though they have been useful for diagnosing aspects of free-shear-flow noise generation and its modeling, have neither illuminated any generally applicable simplifying principles nor pointed to any clear means of noise reduction.

Faced with this, we devised an approach to study free-shear-flow noise reduction directly. Given a numerical solution of the compressible flow equations, we solve the adjoint of the linearized perturbed equations backward in time provide the sensitivity of the noise, as defined quantitatively by an appropriate metric, to changes in control actuation. This sensitivity is used to iteratively improve controls for the selected noise-reduction objective. The scheme is formulated mathematically in section 4.3.

This iterative approach is, however, computationally intense, requiring numerous numerical solutions of the adjoint and flow equation to optimize the controls. For this reason we considered a two-dimensional mixing-layer model of the near-nozzle region of a jet. The details of the mixing layer and its numerical simulation are provided in the following section 4.2. This flow has several of the salient features of a jet, but can be computed at a fraction

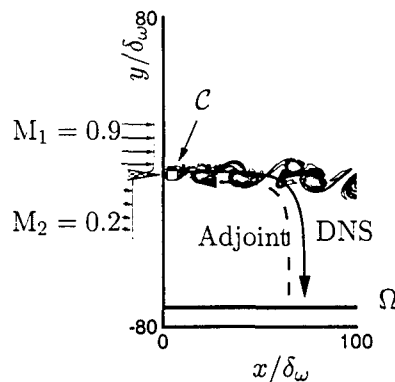


Figure 6: Mixing layer control schematic.

of the expense of even a low-Reynolds-number turbulent jet.³ It is also easier to interpret certain results for this simplified flow model, though care must be taken in generalizing the specific results to three-dimensional, turbulent flows because of their additional complexity.

Clearly, such an iterative scheme is not designed for implementation in hardware, since the iterative process itself requires full knowledge of the unsteady flow field. Instead, we use it to probe the mechanisms of free-shear-flow noise, particularly the noise due to the quasi-two-dimensional (instability wave-like) flow structures in a turbulent flow, and perhaps most importantly to gage how much noise reduction can be accomplished with nozzle controls. (How quiet can it be? What type of control is required?) This study is undertaken in section 4.4, which contains the bulk of this paper's results. Of particular interest are the changes induced by the control. Once a mixing layer's noise is significantly reduced, and it is shown that this results via a genuine change in the flow as a source of sound, we can compare the original noisy flow and its quieted counterpart to illuminate noise mechanisms in a way that has not before been possible.

4.2 The two-dimensional mixing layer

4.2.1 Flow parameters

The mixing layer simulated is shown schematically in figure 6. The velocity difference across the layer is ΔU , with which we can define the inflow vorticity thickness,

$$\delta_\omega = \frac{\Delta U}{|du/dy|_{\max}}, \quad (2)$$

of the initial hyperbolic tangent velocity profile for use as a length scale. This inflow condition simplifies the flow relative to its experimental counterpart by removing any interaction with a splitter plate (or nozzle lip), which can change the character of the acoustic radiation. The flow Reynolds number is $Re_u \equiv \rho_\infty \Delta U \delta_\omega / \mu = 500$ with μ the constant viscosity of the fluid and ρ_∞ the ambient density, which is the same in both streams. We also assume zero bulk viscosity. The Mach numbers of the free streams are $M_1 = U_1/a_\infty = 0.9$ and $M_2 = U_2/a_\infty = 0.2$, where a_∞ is the ambient sound speed. We assume a perfect gas with constant Prandtl number $Pr \equiv c_p \mu / k = 0.7$.

The flow was simulated in a domain extending $100\delta_\omega$ in x and out to $\pm 80\delta_\omega$ in y , as shown

Source type	(f_1, f_2, f_3, f_4)	(f'_1, f'_2, f'_3, f'_4)	(a_2^*, a_3^*)	g
Mass ^a	$(1, 0, 0, T_0/\gamma)$	$(0, 0, 0, 0)$	$(0, 0)$	$\rho^* + p^* T_0/\gamma$
x body force	$(0, 1, 0, u)$	$(0, 0, 0, u')$	$(p^*, 0)$	$u^* + up^*$
y body force	$(0, 0, 1, v)$	$(0, 0, 0, v')$	$(0, p^*)$	$v^* + vp^*$
Int. energy	$(0, 0, 0, 1)$	$(0, 0, 0, 0)$	$(0, 0)$	p^*

^awith zero velocity and temperature $T_0 = 1/(\gamma - 1)$

Table 1: Vectors used for different controls: $\mathbf{F} = [f_1, f_2, f_3, f_4]^T$ defined in (4); $\mathbf{F}' = [f'_1, f'_2, f'_3, f'_4]^T$ defined in (15); $\mathcal{A}^* = [0, a_2^*, a_3^*, 0]^T$ defined in (20); and the gradient $g(\mathbf{x}, t)$ defined in (13).

in figure 6. The line Ω at $y = -70\delta_\omega$ and extending between $x = 0$ and $x = 100\delta_\omega$ was targeted by our control for noise reduction. This one-sided noise reduction objective is inspired by jet noise reduction, which is most important in the downward toward-the-ground direction, though the formulation admits considerable flexibility in selecting Ω . It is possible to select an Ω in the far field, but computing far-field sound and propagating the adjoint solution back into the meshed computational domain would both introduce errors and add considerable complexity. The computational savings of such an approach would be small because most mesh points are in the vortical region of the flow. The controls discussed subsequently were applied only in the small square region labeled \mathcal{C} in the figure, covering $x/\delta_\omega \in [1, 7]$ and $y/\delta_\omega \in [-3, 3]$. Since \mathcal{C} does not span the entire width of the mixing layer that has significant vorticity (see figure 6), we do not anticipate laminarization to be an option for our control.

4.2.2 Governing flow equations

The compressible viscous flow equations were formulated in Cartesian coordinates and are provided in full in appendix A. Here, the equations are presented only in operator form. The compressible flow equations are thus

$$\mathcal{N}(\mathbf{q}) = 0, \quad (3)$$

where \mathbf{q} is a vector of the primitive flow variables $\mathbf{q} = [\rho, u, v, p]^T$.

The control is implemented into the equations as a general source term $\phi(\mathbf{x}, t)$ with compact support in \mathcal{C} (see figure 6):

$$\mathcal{N}(\mathbf{q}) = \mathbf{F}\phi(\mathbf{x}, t), \quad (4)$$

where the vector \mathbf{F} puts the control's action into the different equations that make up \mathcal{N} (see appendix A) and enforces certain consistencies for the control forcing. For example, it is designed so that momentum forcing appears consistently in the momentum equation and in the total energy equation, where it acts on the kinetic energy. Specific \mathbf{F} vectors for the flow equations in appendix A are listed in table 1 for the different types of control considered.

4.2.3 Numerical methods

The flow equations were solved numerically and without any modeling approximations. A fourth-order Runge-Kutta algorithm was used to advance the solution in time. Spatial derivatives were computed with a sixth-order compact finite-difference scheme²¹ in the

x direction and a fourth-order seven-point explicit coefficient-optimized finite-difference scheme²² in the y direction. The explicit scheme in y facilitated domain decomposition for solution on parallel computer systems.

In our computation, the equations were discretized with 960×640 mesh points in the x and y directions, respectively. The mesh was stretched in y to increase the resolution in the shear layer. It had a minimum spacing $\Delta y_{\min} = 0.14\delta_\omega$ at $y = 0$, a maximum spacing $\Delta y_{\max} = 0.96\delta_\omega$ at $y = \pm 80\delta_\omega$, and a maximum stretching rate $|(\Delta y_{i+1} - \Delta y_i)/\Delta y_i|_{\max} = 1.6\%$ at $y \approx \pm 55\delta_\omega$. Beyond the physical domain (see section 4.2.1), the mesh was stretched continuously and extended $60\delta_\omega$ upstream and downstream of the physical domain in x and $20\delta_\omega$ beyond its top and the bottom in y . In these zones, damping with strength increasing away from the physical domain was added to the equations in order to mimic a radiation condition.²³ Specifically, the damping terms appear in the governing equations simply as

$$\mathcal{N}(\mathbf{q}) = -\xi(\mathbf{q} - \mathbf{q}_{\text{target}}), \quad (5)$$

where the damping coefficient ξ is zero in the physical domain and varies quadratically from 0 to $0.2a_\infty/\delta_\omega$ between the physical and the computational domain boundaries. By the time all fluctuations reached the actual boundaries of the computational domain, they were reduced to such a negligible level that standard one-dimensional characteristic boundary conditions adequately absorbed outgoing perturbations.

4.2.4 Inflow excitation

To make the mixing layer well defined and reproducible and to avoid any spurious auto excitation associated with the numerical discretization, we explicitly excited our mixing layer. Another objective of this excitation was to provide a relatively high amplitude disturbance level at the inflow to properly challenge the controller.

Linear instability analysis predicts that the most unstable mode of the corresponding incompressible mixing layer, with the assumption of parallel flow, has Strouhal number $St_0 = f_0\delta_\omega/(4U_c) \approx 0.032$,²⁴ where $U_c = (U_1 + U_2)/2$ and f_0 is the mode's frequency. Thus, frequency f_0 provides an estimate of the fundamental frequency of our compressible mixing layer, since it is not very sensitive to the present compressibility level.²⁵ Numerical experimentation confirmed that our mixing layer does respond most strongly to excitations with frequencies near f_0 .

We excited the flow at a total of eight frequencies,

$$f_i = \frac{f_0}{4}(i + \alpha^{(i)}), \quad i = 1, 2, \dots, 8, \quad (6)$$

where $\alpha^{(i)}$ are uniformly distributed random numbers such that $\alpha^{(i)} \in (-0.5, 0.5)$. In section 4.4.1, we confirm that the noise and its controllability are insensitive to the particular random numbers defining the excitation. For comparison, we also simulated and controlled a mixing layer excited with f_0 , $2f_0$, and 6 subharmonics of f_0 . This excitation, which is similar to that used by,¹⁶ produces a regular roll-up and pairing of vortices (see section 4.4.6).

A special procedure was designed to reduce the direct effect of the excitation on the sound field. We defined

$$\psi = \psi_0 e^{-0.2(x-x_0)^2} e^{-0.2y^2} \sum_{i=1}^8 \sin \left[\frac{2\pi f_i(x - x_0 - U_c t)}{U_c} + \beta_x^{(i)} \right] \sin \left[\frac{2\pi f_i y}{U_c} + \beta_y^{(i)} \right], \quad (7)$$

where $\psi_0 = 0.008\rho_\infty a_\infty^2/\delta_\omega$ and $x_0 = -10\delta_\omega$. The β_x and β_y are random phases $\in [0, 2\pi)$ and are constant for the entire simulation. The excitation was then included as a body force

$$\mathbf{F}_e = \left(\frac{\partial\psi}{\partial y}, -\frac{\partial\psi}{\partial x} \right), \quad (8)$$

which is solenoidal and thus relatively quiet. Our selected x_0 puts the excitation upstream of the physically realistic portion of the computation. The ξ in (5) has maximum value of only $0.0125a_\infty/\delta_\omega$ in this region, which does counteract the excitation but does not significantly interfere with its objectives.

This approach can generate disturbances at the physical domain boundary that are higher amplitude than could be accurately prescribed locally at the inflow boundary without generating spurious sound. The average turbulence intensity at the center of the control region ($x = 4\delta_\omega$, $y = 0$) close to the inflow was already 70% of its peak value further downstream. The excitation \mathbf{F}_e appears in the momentum equations, but has support only for $x < 0$, which is the beginning of what we consider the physical domain. Therefore, for clarity we omit it from subsequent analysis. Its purpose is solely to provide an inflow condition. Our controller, of course, has no direct knowledge of this excitation. Because the base flow is a slowly spreading shear layer, the noise from excitation is not expected to be exactly zero, but both visualizations and the eventual success of the control show that it is negligible relative to the physical noise from the mixing layer.

4.2.5 Simulation procedure

To avoid initial transients, we first simulated the flow for time $588\delta_\omega/\Delta U$, which is approximately 59 fundamental vortex roll-up periods according to our estimated f_0 . This process took 10 500 numerical time steps with $\Delta t = 0.056\delta_\omega/\Delta U$. Then the control was applied for $437.5\delta_\omega/\Delta U$ time units, which is about 44 fundamental roll-up periods. Figure 7 (a) shows the flow and sound fields, which include data in two regions: the direct numerical simulation data (inner area) and a far-field acoustic extrapolation beyond the simulation domain, which was computed as by.³ It is seen in figure 7 (b) that the target line Ω at $y = -70\delta_\omega$ is indeed in the far acoustic field, as defined for this purpose by a $1/r$ intensity decay. This supports our approach of using the pressure data on Ω to control the far-field sound.

4.3 Control formulation

4.3.1 The control and its objective

The control objective is to make the mixing layer as quiet as possible with local actuation near the inflow, which will allow us to study noise mechanisms effectively and establish an empirical lower bound on the mixing layer's noise. Thus, it is desirable to have the most general control possible, which in our simulation methodology corresponds to treating each space-time point of the discrete representation of $\phi(\mathbf{x}, t)$ in (4) as an independent control parameter. In the reported results, the function ϕ is discretized over a 36×45 point subregion of the simulation mesh in \mathcal{C} for 7812 time steps, giving approximately 10^7 control parameters to be optimized. (The much smaller number of control dimensions actually necessary for control is investigated in section 4.4.5.)

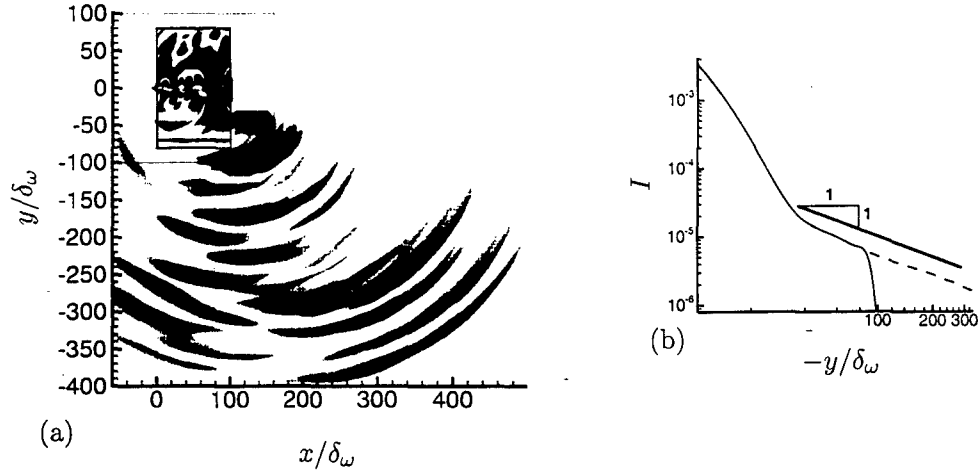


Figure 7: (a) Visualization of the flow and sound field before control. The rectangular boxes outline the physical and total (including boundary zones) computational domains. (b) Sound intensity $(p - \bar{p}_o)^2 / \rho_\infty^2 a_\infty^4$ on $x = 94\delta_\omega$: flow simulation data — (the sudden drop near $x = 100\delta_\omega$ corresponds to the absorbing boundary zone) and acoustic extrapolation data ----.

The control's specific objective is to reduce noise as defined by the cost functional

$$\mathcal{J}(\phi) = \int_{t_0}^{t_1} \int_{\Omega} [p(\phi(\mathbf{x}, t), \mathbf{x}, t) - \bar{p}_o(\mathbf{x})]^2 d\mathbf{x} dt, \quad (9)$$

where t_0 and t_1 are the start and end times of the control period, p is the local pressure, which can be viewed to depend upon the control $\phi(\mathbf{x}, t)$, and \bar{p}_o is the spatially dependent but time averaged pressure before control is applied. This mean pressure is nearly uniform on Ω with $|\bar{p}_o - p_\infty| < 0.0017p_\infty$, where p_∞ is the nominal ambient pressure, but since this variation is comparable with the uncontrolled acoustic pressure fluctuations ($\approx 0.003p_\infty$), this difference of the mean pressure from the pressure at infinity is important for properly defining the sound. The mean pressure of the controlled cases, \bar{p} , is not constrained, and in principle can drift due to the control, though any such drift would be penalized by increasing \mathcal{J} . We observe, however, that the difference in \bar{p} from \bar{p}_o on Ω is less than 3% of the maximum uncontrolled acoustic pressure fluctuations, so $\mathcal{J}(\phi)$ in (9) effectively remains acoustic when control is applied.

4.3.2 Sensitivity

To determine the sensitivity of the cost functional \mathcal{J} to small modifications of the control ϕ , we consider the perturbation \mathcal{J}' that results from an arbitrary perturbation ϕ' to the control ϕ . This perturbation \mathcal{J}' is defined as a differential of the cost functional \mathcal{J} with respect to $\phi(\mathbf{x}, t)$ in the direction ϕ' :

$$\mathcal{J}' \equiv \lim_{\varepsilon \rightarrow 0} \frac{\mathcal{J}(\phi + \varepsilon\phi') - \mathcal{J}(\phi)}{\varepsilon} = \int_{t_0}^{t_1} \int_{\Omega} 2[p(\phi, \mathbf{x}, t) - \bar{p}_o(\mathbf{x})]p'(\mathbf{x}, \phi, \phi') d\mathbf{x} dt. \quad (10)$$

The limit that defines p' in the integrand is exactly analogous to that which defines \mathcal{J}' . In forming the rightmost term in (10) from (9), the derivative operation can be viewed as

commuting with the integration operation. With the differential of the functional \mathcal{J} defined in (10), the gradient $g(\phi)$ of the functional \mathcal{J} for any direction ϕ' can be defined implicitly as

$$\mathcal{J}' = \int_{t_0}^{t_1} \int_C g(\phi) \phi' \, d\mathbf{x} dt. \quad (11)$$

The space integration in (11) is only over C , the support of ϕ' . Together (10) and (11) provide an implicit formula for g ,

$$\int_{t_0}^{t_1} \int_C g(\phi) \phi' \, d\mathbf{x} dt = \int_{t_0}^{t_1} \int_{\Omega} 2[p(\phi, \mathbf{x}, t) - \bar{p}_o(\mathbf{x})] p'(\mathbf{x}, \phi, \phi') \, d\mathbf{x} dt, \quad (12)$$

which in principle could be solved for the best ϕ' if all p' were known for all potential ϕ' perturbations, but to solve for the n space-time components of ϕ' , we would need to solve the flow at least n times for n linearly independent perturbations. For large n (10^7 in our case), this option is impractical. In the next section, we use an adjoint formulation to solve for g directly, which can then be used to update the control by

$$\phi^{\text{new}} = \phi^{\text{old}} + r g(\phi^{\text{old}}), \quad (13)$$

where r is a generalized distance in ϕ coordinates determined iteratively to minimize $\mathcal{J}(\phi^{\text{new}})$ in the g direction.

4.3.3 Adjoint-based optimization: formulation

Our formulation is similar to that of⁴ for incompressible flow and we use similar notation. As in (10), a differential is applied to all flow variables \mathbf{q} , to define $\mathbf{q}' = [\rho' \, u' \, v' \, p']^T$. We take \mathbf{q}' to be the still unknown perturbation to a solution \mathbf{q} of the flow equations (4) due to a control perturbation ϕ' , though this specific designation is not assumed by the differential definition of \mathbf{q}' . Mathematically, this means that

$$\mathcal{N}(\mathbf{q} + \mathbf{q}') = \mathbf{F}(\mathbf{q} + \mathbf{q}')(\phi + \phi'), \quad (14)$$

where the notation for the term on the right side indicates that the vector \mathbf{F} depends on $\mathbf{q} + \mathbf{q}'$ and multiplies the scalar $\phi + \phi'$. Linearizing (14) in \mathbf{q}' , or equivalently taking the differential of the governing equation (4), yields

$$\mathcal{N}'(\mathbf{q})\mathbf{q}' = \mathbf{F}'\phi + \mathbf{F}\phi'. \quad (15)$$

The operation $\mathcal{N}'(\mathbf{q})\mathbf{q}'$ is linear in \mathbf{q}' , though $\mathcal{N}'(\mathbf{q})$ is itself a nonlinear function of \mathbf{q} . It is convenient for the subsequent development to define

$$\mathcal{M}'(\mathbf{q}, \phi)\mathbf{q}' = \mathcal{N}'(\mathbf{q})\mathbf{q}' - \mathbf{F}'\phi = \mathbf{F}\phi', \quad (16)$$

thus isolating the control perturbation on the right side of the equation. The \mathbf{F}' corresponding to the specific controls we consider are listed in table 1.

With an inner product defined

$$\langle \mathbf{c}, \mathbf{d} \rangle \equiv \int_{t_0}^{t_1} \int_{\mathbb{R}^2} \mathbf{c} \cdot \mathbf{d} \, d\mathbf{x} dt \equiv \int_{t_0}^{t_1} \int_{\mathbb{R}^2} \sum_{n=1}^4 c_n(\mathbf{x}, t) d_n(\mathbf{x}, t) \, d\mathbf{x} dt, \quad (17)$$

the adjoint of $\mathcal{M}'(\mathbf{q})$ is obtained by integration by parts:

$$\langle \mathcal{M}'(\mathbf{q})\mathbf{q}', \mathbf{q}^* \rangle = -\langle \mathbf{q}', \mathcal{M}^*(\mathbf{q})\mathbf{q}^* \rangle + b. \quad (18)$$

where b includes the space and time boundary terms (see equation 21 below) and

$$\mathbf{q}^* = [\rho^* \ u^* \ v^* \ p^*]^T \quad (19)$$

is introduced as the adjoint field. The adjoint operator \mathcal{M}^* includes two parts:

$$\mathcal{M}^*(\mathbf{q})\mathbf{q}^* = \mathcal{N}^*(\mathbf{q})\mathbf{q}^* + \mathcal{A}^*(\mathbf{q}^*)\phi. \quad (20)$$

The term $\mathcal{A}^*(\mathbf{q}^*)$ arises from \mathbf{F}' in (16) and is nonzero only for certain cases, as indicated in table 1. The term $\mathcal{N}^*(\mathbf{q})\mathbf{q}^*$ is derived from the flow equations (see appendix B) and is the same for all controls considered.

The boundary term b in (18) is

$$b = \iint_{t_0}^{t_1} (B_x \mathbf{q}') \cdot \mathbf{q}^* \Big|_{x=-\infty}^{x=+\infty} dt dy + \iint_{t_0}^{t_1} (B_y \mathbf{q}') \cdot \mathbf{q}^* \Big|_{y=-\infty}^{y=+\infty} dt dx + \int_{\mathbb{R}^2} (B_t \mathbf{q}') \cdot \mathbf{q}^* \Big|_{t_0}^{t_1} dx, \quad (21)$$

where the B factors are 4×4 matrices. This boundary term b can be eliminated by choosing appropriate boundary and initial conditions for the adjoint problem. Mathematically, causality insures that the first two integrals are zero for the finite time interval considered here. However, since the physical domain of the computation was necessarily finite, an effectively equivalent radiation-like condition was enforced at the numerical boundary. This condition was implemented in practice as in the flow solution with a combination of characteristic boundary conditions and an absorbing boundary zone. Causality also eliminates the time boundary term at the initial time $t = t_0$ in the third integral: there can be no perturbation to the flow (*i.e.* $\mathbf{q}' = 0$) due to the control before the control is applied. The condition at the end time $t = t_1$ can be eliminated by simply starting with $\mathbf{q}^* = 0$ at $t = t_1$ and solving the adjoint system backward in time.

We can now choose a source term \mathbf{F}^* for our adjoint system,

$$\mathcal{M}^*(\mathbf{q})\mathbf{q}^* = \mathbf{F}^*, \quad (22)$$

so that the adjoint solution provides the gradient g in (13). We start by substituting (16) and (22) into (18) with $b = 0$ as discussed to show that

$$\langle \mathbf{F}\phi', \mathbf{q}^* \rangle = -\langle \mathbf{q}', \mathbf{F}^* \rangle. \quad (23)$$

Comparing (23) with (12), we would like

$$-\langle \mathbf{q}', \mathbf{F}^* \rangle = \int_{t_0}^{t_1} \int_{\Omega} 2[p(\phi, \mathbf{x}, t) - \bar{p}_o(\mathbf{x})]p'(\mathbf{x}, \phi, \phi') d\mathbf{x} dt, \quad (24)$$

so that

$$\langle \mathbf{F}\phi', \mathbf{q}^* \rangle = \int_{t_0}^{t_1} \int_{\mathcal{C}} g(\phi)\phi' d\mathbf{x} dt. \quad (25)$$

The adjoint source term \mathbf{F}^* that gives (24) from (17) is

$$\mathbf{F}^* = \begin{bmatrix} 0 & 0 & 0 & -2(p - \bar{p}_o) \int_{\Omega} \delta(\mathbf{x} - \mathbf{x}_o) d\mathbf{x}_o \end{bmatrix}^T, \quad (26)$$

and by (25)

$$g(\phi) = \mathbf{F} \cdot \mathbf{q}^*, \quad (27)$$

where, in practice, q^* is known from the numerical solution of the adjoint system and \mathbf{F} is case dependent and defined in table 1. With $g(\phi)$, we now have the generalized direction in which to change ϕ to reduce \mathcal{J} for use in a gradient-based optimization procedure.

4.3.4 Adjoint-based optimization: numerical implementation

The adjoint equations are solved on the same mesh and by the same methods used to solve the flow equations. The δ -function in (26) is distributed to the computational mesh by a Gaussian distribution function $e^{-(y+70\delta_\omega)^2/(4\Delta y^2)}$, where Δy is the local mesh spacing. Thus, our smeared out approximation to the δ -function has width $\approx 2.7\delta_\omega$, which is much less than the wavelength ($\gtrsim 14\delta_\omega$) of any significant radiated sound waves. This was proven to be effective in noise cancellation tests.¹⁷

For the control update, the Polak–Ribiere variant of the conjugate gradient algorithm is used with Brent’s line minimization.²⁶ Each line minimization typically required approximately 10 flow solutions and 10 adjoint solutions. One entire line-minimization procedure, which accomplishes the step along one conjugate gradient, is designated as one iteration in the following, so the number of field solutions can be estimated as $\approx 20 \times (\# \text{ iterations})$, but this approximate number is, of course, sensitive to the local shape of $\mathcal{J}(\phi)$. All optimizations were started from a $\phi = 0$ condition, which may be responsible for the particular optimized conditions found by the control because standard gradient descent searches can only find local minima. Since the success of our control is sufficient to study noise mechanisms of interest, we have not investigated this possibility.

As shown in section 4.3.3, the entire flow-field solution needs to be saved in order to solve the adjoint equations. To save memory and minimize data input and output operations, we saved the flow solutions only at every other point in space and time and interpolated using third-order polynomials in space and linear interpolation in time. No differences were noted between test cases computed using the full fields and the interpolated fields. The optimizations presented in this paper each required approximately 20,000 processor-hours of computation on an IBM SP3, usually using 80 processors and requiring about 30 gigabytes of memory.

4.3.5 Adjoint solution

The evolution of the adjoint pressure p^* is visualized in figure 8. It is this quantity that provides the gradient information g to update the internal-energy control and is a factor in all the types of control studied (see table 1). Since the flow equations are self-adjoint in the acoustic limit, the adjoint pressure starts out as an adjoint sound wave, excited along Ω by the pressure as specified in (26). When this wave encounters the mixing layer, it excites disturbances that convect upstream in the shear layer in a way similar (but time reversed) to the motion of the vortex structures of the flow field, and with approximately the same speed as the structure convective Mach number, $M_c = 0.55$. These disturbances eventually reach \mathcal{C} , where the adjoint solution provides the gradient g to update ϕ according to (27). These observations suggest that the effect of the control follows the same track but in reverse from \mathcal{C} to the target line Ω . They also suggest that the control mechanism is via the instabilities and flow structures in the mixing layer, and not so-called anti-sound acoustic cancellations,

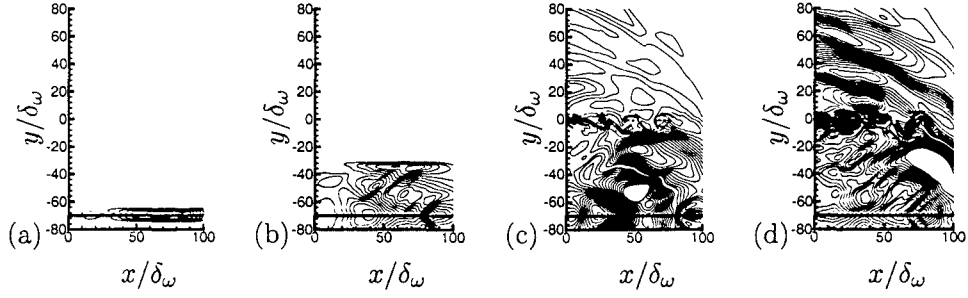


Figure 8: Adjoint pressure p^* : (a) $t = 435.1\delta_\omega/\Delta U$, (b) $t = 411.6\delta_\omega/\Delta U$, (c) $t = 294\delta_\omega/\Delta U$, (d) $t = 235.2\delta_\omega/\Delta U$. The time decreases in the adjoint solution.

an issue that is revisited in detail in section 4.4.2. Given this qualitative behavior of the adjoint, we can express the expected mechanism of noise control as follows: (1) the control interacts with the flow, (2) this interaction alters (slightly, as we shall see) the instabilities in the flow, and (3) the modified flow is quieter. This interpretation will be strengthened quantitatively in section 4.4.

4.3.6 Price term

It should be noted that the cost \mathcal{J} in (9) does not penalize the control effort. A term to do this was intentionally omitted since our primary objective is to study the effect of the control on the flow and its noise mechanism, not to seek any mathematically formal optimum. Such an objective would probably require a price term added to (9) that penalizes the control effort:

$$\mathcal{H}(\phi) = \mathcal{J}(\phi) + c_w \int_0^T \int_C \phi^2 dx dt. \quad (28)$$

The gradient to reduce \mathcal{H} is then

$$g(\phi) = \mathbf{F} \cdot \mathbf{q}^* + 2c_w \phi. \quad (29)$$

Numerical results for this formulation are provided by.¹⁷ Though the control effectiveness is, of course, reduced for large enough c_w , all of the following conclusions are unchanged by the price term. Pertinent observations on the price term's effect are noted in the following. In section 4.4.3, we will briefly discuss its effect on the spectrum of the control and in section 4.4.4 we will mention that it is responsible for increasing the streamwise integral length scale of the control.

4.4 Results

4.4.1 Sound reduction

Figure 9 shows the reduction of \mathcal{J} by different types of control. To make this plot, we increased the starting point t_0 in the cost function (9) by the acoustic travel time from \mathcal{C} to the nearest point on Ω . This approximation provides a lower bound on the time at which the control will be effective on Ω . Before this time, \mathcal{J} not reducible from \mathcal{C} , but for a period even after this adjusted t_0 , the sound on Ω is not fully controllable for two reasons: (1) the control's effect can only reach the closest point on Ω , and (2) the rate at which the control's effect travels within the mixing layer is slower than the sound speed. In the layer,

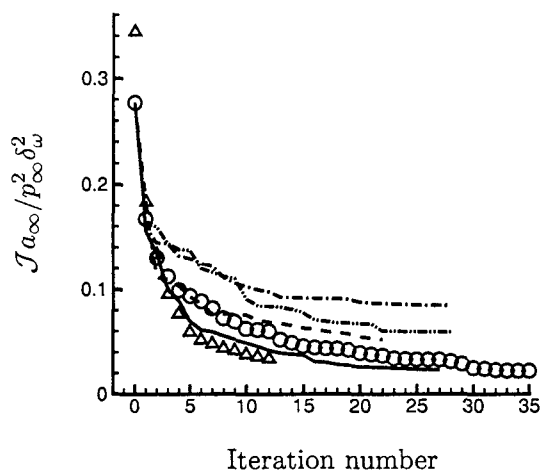


Figure 9: The reduction of the cost function by different controls: mass; x -direction body force ----; y -direction body force -.-.-; internal energy ———; and all-terms control \bigcirc . The Δ show internal energy control for the same flow but with different random number excitation in (6) and (7).

it is expected to travel at approximately the structure convective Mach number, $M_c \approx 0.55$, as suggested by the adjoint solution behavior seen in section 4.3.5. With this definition, all controls reduced the noise on the target line more than 60%, with the internal-energy control showing a 92% (11 dB) sound reduction. A case with the mixing layer excited by a different set of random numbers $\alpha^{(i)}$ is also shown in this figure to demonstrate insensitivity to the specifics of the artificial random excitation.

We also tried to maximize controllability by combining all four types of control simultaneously. In this case, the control space is 4 times larger than the original one, so we generalize the control to be $\phi_i(\mathbf{x}, t)$ for $i = 1, 2, 3, 4$ and use corresponding \mathbf{F}_i to represent each of the \mathbf{F} vectors in table 1, so (4) becomes

$$\mathcal{N}(\mathbf{q}) = \sum_{i=1}^4 \mathbf{F}_i \phi_i(\mathbf{x}, t). \quad (30)$$

The corresponding cost-function reduction is also shown in figure 9. It is decreased more slowly for the selected optimization parameters than, say, the internal-energy control only, but eventually it approaches about the same control effectiveness. (No attempt was made here or throughout to attach any particular significance to the rate of convergence.) Since the all-terms control offered no clear benefit, we do not discuss it in the rest of this paper and study the four single-equation control types separately.

The sound further from the mixing layer has, of course, been reduced as well, mostly in, but not limited to, the sideline direction targeted by the selected Ω . Figure 10 shows the initial and controlled directivity on a circular arc centered at $x = 50\delta_\omega$ and $y = 0$ with radius $R = 300\delta_\omega$. The greatest reduction is in the acoustic shadow of Ω , between $\alpha = 54^\circ$ and 126° . For smaller and larger α , the control's effectiveness is diminished, though the noise is still reduced. Intensity at angles $\alpha, \beta < 40^\circ$ and $> 140^\circ$ were not computed because they were determined by testing with known sources to be inaccurate in the far

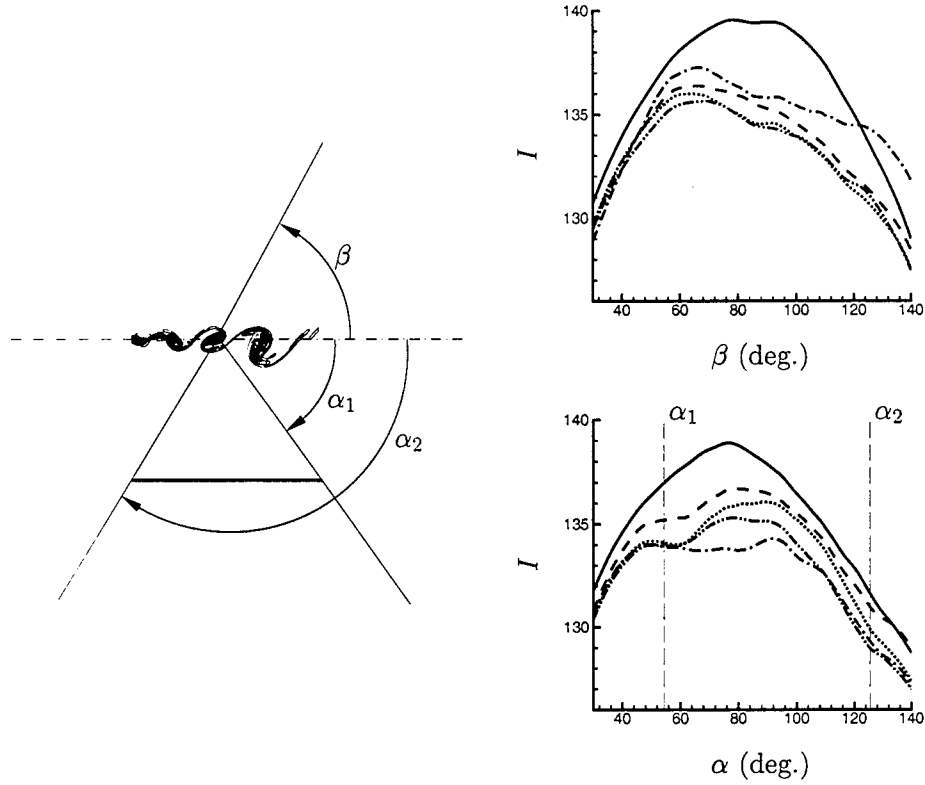


Figure 10: Sound directivity: without control —; and with mass ·····, x -direction body force ----, y -direction body force - · - ·, and internal energy - · - · - controls.

field. Surprisingly, the noise is reduced at all angles, even in the opposite direction to that targeted by our choice of Ω . This overall reduction is inconsistent with any simple anti-sound noise cancellation mechanisms, which is investigated in detail next.

4.4.2 Anti-sound?

Before proceeding to investigate the effects of the control on the flow, it is important to establish quantitatively that the noise reduction is indeed by a change in the flow as a source of sound and not an anti-sound acoustic cancellation with ϕ in \mathcal{C} providing the canceling acoustic waves. It was already suggested in section 4.3.5 that since adjoint instability waves dominate the gradient information in \mathcal{C} , the control mechanism should be linked to the hydrodynamics.

To demonstrate further that our control is not by anti-sound and is, in fact, far superior to what could be accomplished with anti-sound, we designed the numerical experiment shown in figure 11 (a). Here, \mathcal{C} is moved away from the shear layer such that it is now defined by $x/\delta_\omega \in [1, 7]$ and $y/\delta_\omega \in [-21, -15]$. The adjoint instability wave never reaches this control region, so control should be principally by acoustic cancellation. Only the internal-energy source control, which can be an efficient monopole-like sound source, is presented here for demonstration purposes. After 12 iterations, a 40% reduction is observed (figure 11 b), which is not surprising because anti-sound is known to be effective locally, though it is also

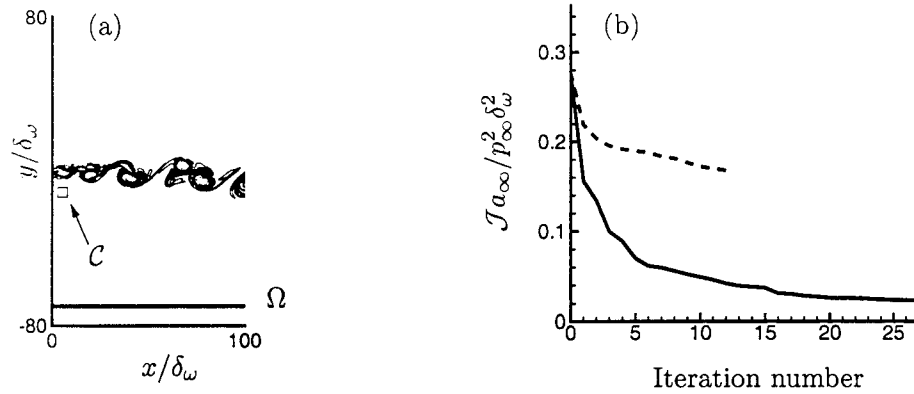


Figure 11: Anti-sound control test: (a) configuration schematic; (b) the reduction of \mathcal{J} by internal energy source control in the shear layer — (from figure 9) and off the shear layer ----.

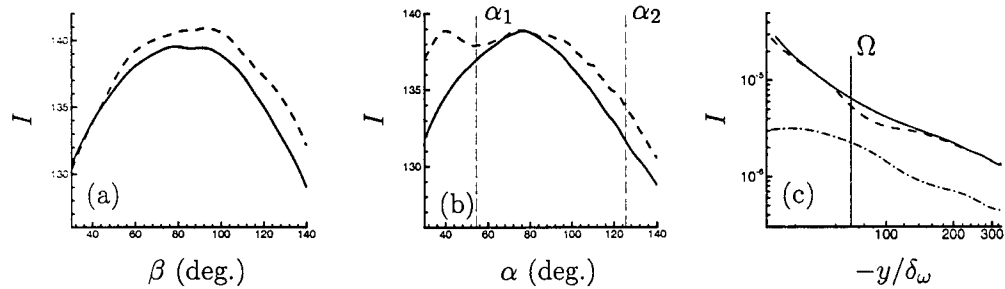


Figure 12: Plots (a) and (b) show sound directivity: without control — and with internal energy anti-sound control ----, with α and β defined in figure 10. (c) Sound intensity on the line $x = 94\delta_\omega$: without control —, with anti-sound control ----, and with internal energy control in the shear layer -.-.-.

known to increase the sound elsewhere. Figures 12 (a) and (b) show the sound directivity of this case. The anti-sound control case is actually louder than the case without control in most directions. Even for the area in the acoustic shadow of Ω , there is no far-field sound reduction. Figure 12 (c) suggests that the non-collocated flow and control noise sources produce local cancellation on Ω but not beyond. Clearly, the flow control is more effective than would seem possible for just anti-sound, though we can not rule out the possibility that an anti-sound mechanism might aid it. We saw in figure 10 that the control is not as successful in the far field as on Ω , which suggests that the noise reduction on Ω might indeed include some anti-sound component.

4.4.3 Spectra

There are four important spectra in our controlled flow. The first is of our randomized excitation based on the estimated fundamental frequency f_0 , as described in section 4.2.4. Unless otherwise noted, the particular random numbers used gave excitation frequencies $0.36f_0$, $0.40f_0$, $0.69f_0$, $0.99f_0$, $1.28f_0$, $1.57f_0$, $1.86f_0$, and $1.90f_0$. The second is the spectrum of the optimized control; the third is the near-field spectrum of the mixing layer before and after control is applied; and the fourth is the spectrum of radiated sound before and after control. Figure 13 shows all these spectra.

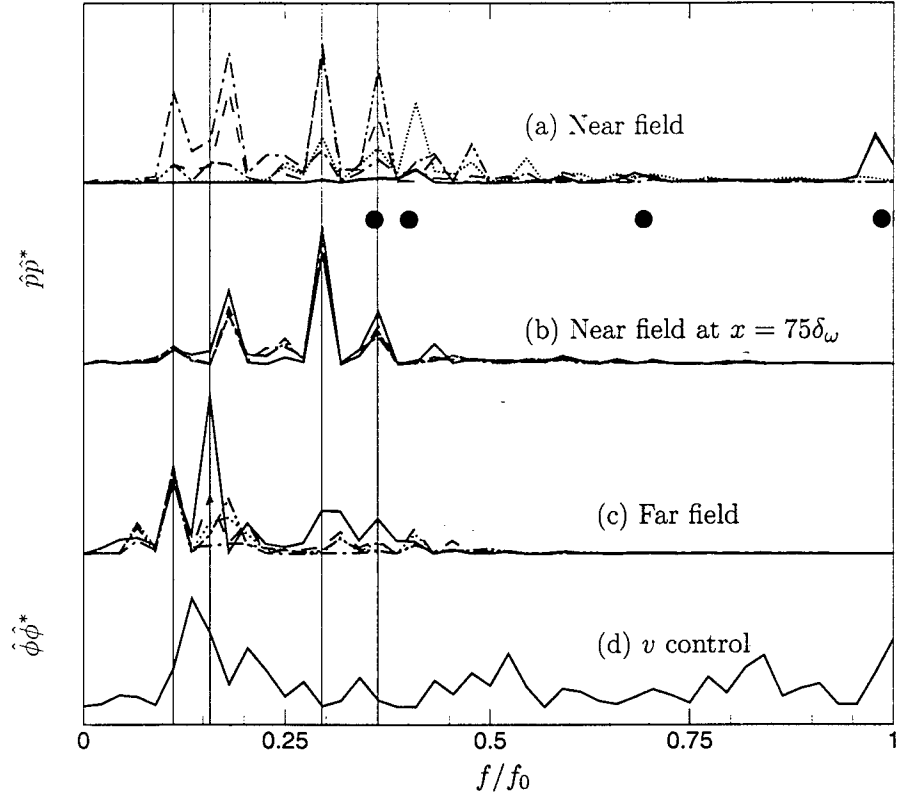


Figure 13: Flow and control spectra. (a) Near-field ($y = 0$) pressure spectra $\hat{p}\hat{p}^*$. The — line shows the overlaid controlled cases and uncontrolled cases at $x = 4\delta_\omega$, the center of \mathcal{C} . The no control case is also shown at $x = 25\delta_\omega$ ·····, $x = 50\delta_\omega$ ·····, $x = 75\delta_\omega$ ----, and $x = 100\delta_\omega$ ····· . (b) Pressure spectra $\hat{p}\hat{p}^*$ at $x = 75\delta_\omega$, $y = 0$ without control —; and with mass ·····, x -direction body force ----, y -direction body force ----, and internal energy ····· controls. The same cases are shown with the same line types in (c) for the far-field sound pressure spectra $\hat{p}\hat{p}^*$ at $x = 152.6\delta_\omega$, $y = -281.9\delta_\omega$ ($\alpha = -70^\circ$ on the same arc as in figure 10, which is near the angle of maximum intensity). (d) The spectrum of the optimized y -direction body-force control $\hat{\phi}\hat{\phi}^*$ at $x = 4\delta_\omega$, $y = 0$. Other controls show similar behavior. For reference, the filled circles • mark the four lowest excitation frequencies. The vertical scale is linear but arbitrary for each set of spectra. Curve sets (a) through (c) are nearly flat for $f > f_0$.

At the center of \mathcal{C} , just downstream of the random excitation, the dominant frequency is near f_0 (see the ‘a’ curves in the figure), apparently a direct response to the randomly selected $0.99f_0$ excitation. The control is seen to have an imperceptible effect upon the pressure spectra in \mathcal{C} , showing its weak effect on the hydrodynamics. Downstream, dominant frequencies are lower as expected, and more sensitive to the control as seen in the (b) curves, though the modest changes observed do not suggest any fundamental change to the flow. It is also noteworthy that the near-field spectrum at $x = 75\delta_\omega$ is dominated by frequencies that are significantly lower than the excitation frequencies, suggesting that nonlinear interactions are responsible for their character.

The optimized control (labeled ‘d’ in the figure) has energy over a wide range of frequencies, not just near the sound frequencies it is designed to control. This observation suggests that the control works through the nonlinear dynamics in the mixing layer, not by simply exciting a linear instability that somehow cancels the physical noise, for example. Adding a price

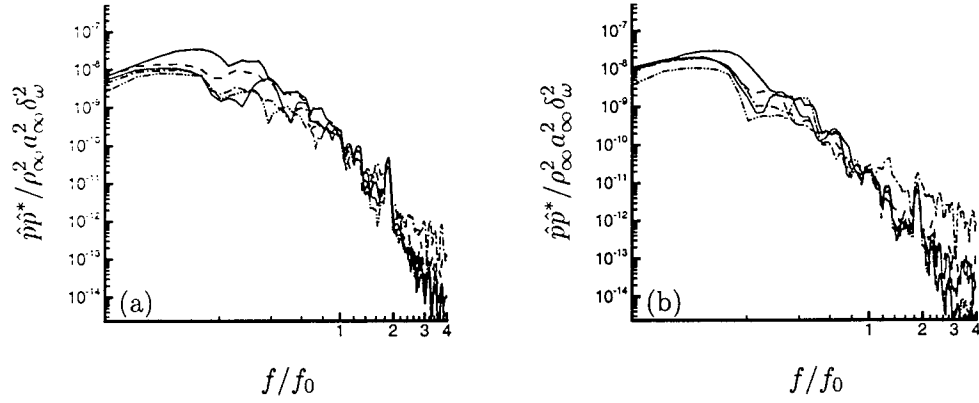


Figure 14: Sound pressure spectra on the same arc as in figure 10 at (a) $\alpha = 50^\circ$ and (b) $\alpha = 90^\circ$: without control —; and with mass ·····, x -direction body force -·-·-, y -direction body force ----, and internal energy -·-·- control.

term to the cost functional, as discussed in section 4.3.6, reduced the control's amplitude at all frequencies, suggesting that they are all important.

The far-field noise spectra are significantly changed by the control. Interestingly, all controls seem to affect spectra in about the same way, reducing mostly a particularly loud peak at $f \approx 0.159f_0$. This peak corresponds to neither a spectral peak in the near-field pressure nor a clear spectral peak in the optimized control. The changes to the complete far-field noise spectrum by different controls are more clearly represented in figure 14. The effect of all controls is to reduce the noise of lower frequencies, which contain most of the acoustic energy, with greater reduction noted closer to the downstream axis. We also see, however, that more high-frequency noise is radiated by the controlled cases. The internal-energy control caused the greatest increase in high frequencies, though it also reduced the overall noise the most.

The apparent success of the controls at some sound frequencies but not others is investigated further in figure 15, which shows directivities in narrow frequency bands for all cases. We see again that the sound is most reduced near the frequency $0.159f_0$, which is the loudest in the uncontrolled case. It is also seen in figures 15 (b) through (d) that the controls are extremely successful at certain angles so that relatively silent angles are formed, suggesting some higher degree of cancellation in the sound source. A similar angle of extinction has been predicted by⁸ for the sound produced by the amplification and decay of instability waves in the shear layers of a jet, and was observed experimentally²⁷ in a round jet experiment and in simulations of regularly forced two-dimensional¹⁶ and axisymmetric²⁸ free shear flows. In all these cases, the flows were excited with a single-frequency or several harmonics. Our randomly excited flow shows no such angles of extinction, and it is well known that turbulent jets do not either. This is the first indication of several that we will investigate in the remainder of the paper that the control has induced a subtle ordering, which, at least as far as acoustics are concerned, shares characteristics with idealized or regularly forced flows.

We can make a preliminary assessment of this suggested similarity by comparing the control

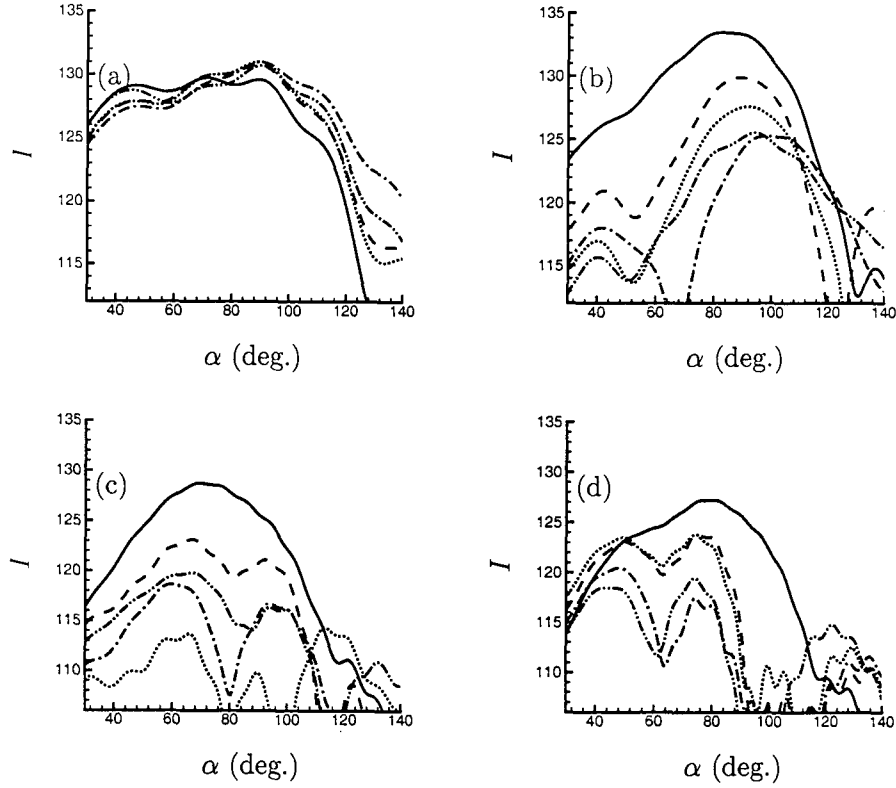


Figure 15: Frequency dependent directivity for frequencies bands (a) $0.093 < f/f_0 < 0.133$, (b) $0.139 < f/f_0 < 0.179$, (c) $0.275 < f/f_0 < 0.315$, and (d) $0.343 < f/f_0 < 0.383$: without control —; and with mass ·····, x -direction body force - · - ·, y -direction body force ----, and internal energy - · - · control. Angle α is defined in figure 10.

of the randomly excited mixing layer to that of the corresponding harmonically excited mixing layer discussed in section 4.2.4. In this case, the noise is not reduced significantly by the control (figure 16). More remarkably, its level nearly matches the noise control limit observed in the randomly excited case. Increasing the amplitude of the harmonic excitation increases the sound level somewhat but does not increase the effectiveness of our control scheme. By the same reasoning that ordering reduces sound, taking $\alpha^{(i)} = 0$ in (6) should also lead to a quieter flow. Indeed, the initial \mathcal{J} in this case falls half way between the random $\alpha^{(i)}$ case and the harmonically excited case. These observations suggests that the harmonically excited flow is pathologically quiet and that it might, in some sense, be near some lower bound on the noise from this type of unsteady free shear flow, though this is beyond the capabilities of our formulation to prove. Further discussion of these similarities is in section 4.4.6.

4.4.4 The optimized control

Figure 17 shows snapshots of the ϕ in \mathcal{C} for various controls at the same time. The apparent structures we see in ϕ can be shown with space-time correlations to advect at the flow's convection speed, though the integral length scale of the control is shorter than the flow. It is also noteworthy that the internal-energy control has a somewhat longer streamwise

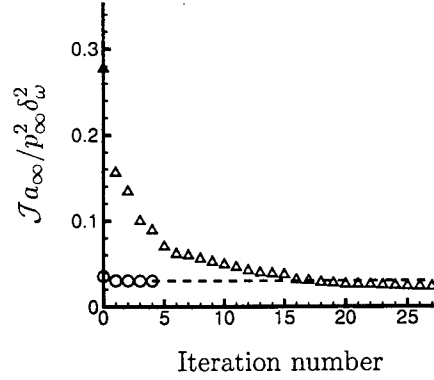


Figure 16: The cost reduction by internal energy control in for the randomly \triangle and harmonically \circ excited mixing layers.

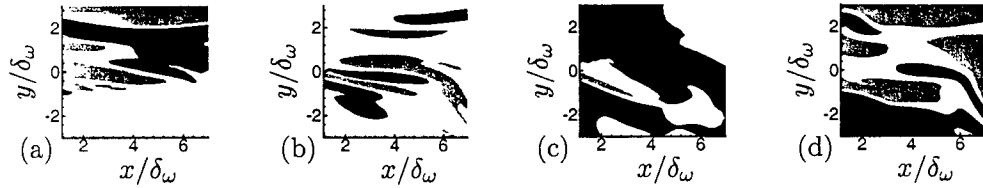


Figure 17: The optimized control ϕ at time $100\delta_\omega/a_\infty$: (a) mass control; (b) x -direction body-force control; (c) y -direction body-force control; and (d) internal energy control. Black indicates $\phi > 0.001$, and gray indicates $\phi < -0.001$ in (a) through (c). These limits are ± 0.01 in (d).

correlation length scale than the other controls.¹⁷ If a price term is added to the cost functional, as discussed in section 4.3.6, the streamwise correlation of the control is seen to increase somewhat,¹⁷ which suggests that the more important components of the control are more downstream persistent.

The power needed by the controls is remarkably small. To show this, a relative power function $\eta(t)$ can be defined as a ratio of the control's power to the turbulence kinetic energy flux through a vertical line \mathcal{L} at the downstream edge of \mathcal{C} ($x/\delta_\omega = 7$, $-80 < y/\delta_\omega < 80$). The instantaneous flux is

$$\tilde{F} = \int_{\mathcal{L}} E_k(x_0, y, t) u(x_0, y, t) dy, \quad (31)$$

with

$$E_k = \frac{1}{2} \rho [(u - \bar{u})^2 + (v - \bar{v})^2], \quad (32)$$

so relative power η for the different cases are defined as

$$\eta_\rho(t) = \frac{1}{\tilde{F}} \int_{\mathcal{C}} \phi_\rho(x, y, t) T_0 / \gamma d\mathbf{x}, \quad (33)$$

$$\eta_u(t) = \frac{1}{\tilde{F}} \int_{\mathcal{C}} \phi_u(x, y, t) u(x, y, t) d\mathbf{x}, \quad (34)$$

$$\eta_v(t) = \frac{1}{\tilde{F}} \int_{\mathcal{C}} \phi_v(x, y, t) v(x, y, t) d\mathbf{x}, \quad (35)$$

	$ \eta_\rho $	$ \eta_u $	$ \eta_v $	$ \eta_e $
Maximum	2.25×10^{-2}	5.13×10^{-3}	1.90×10^{-4}	2.27×10^{-1}
Average	1.94×10^{-3}	4.39×10^{-4}	1.87×10^{-5}	2.75×10^{-2}

Table 2: The maximum and average power needed by controls in terms of relative power ratio function $|\eta|$.

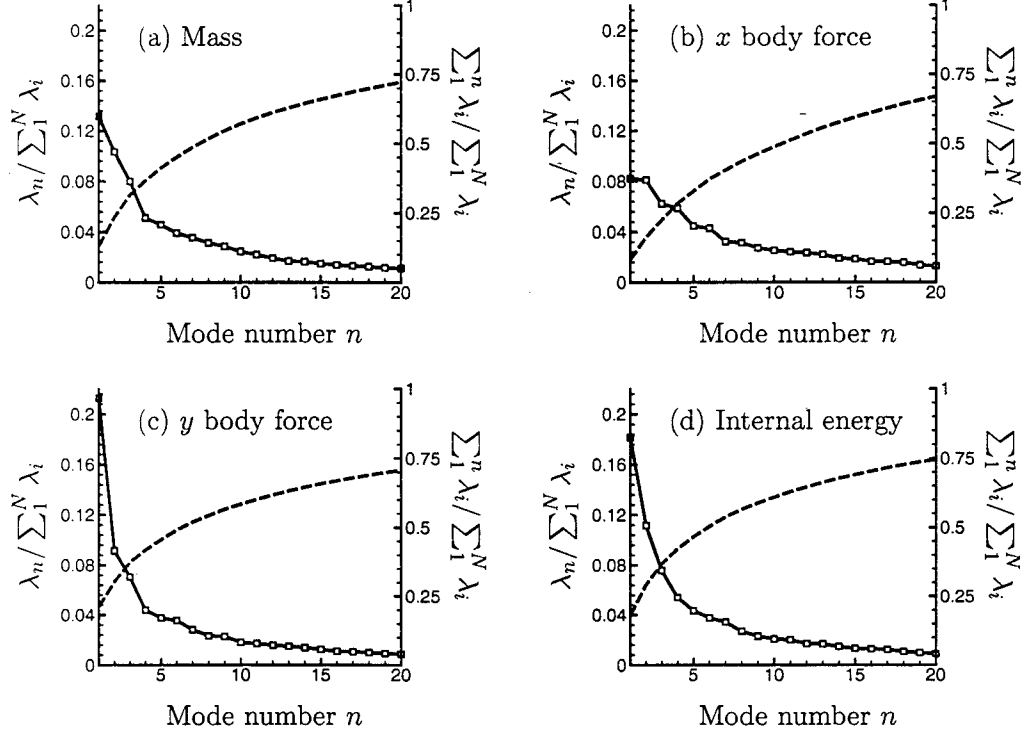


Figure 18: Energy of different basis modes λ_i normalized by the sum $\sum_1^N \lambda_i$. The — lines show energy of each mode (left axis), and ---- lines show energy sum of the first n modes (right axis) for: (a) mass source, (b) x -direction body force, (c) y -direction body force, and (d) internal energy source controls.

and

$$\eta_e(t) = \frac{1}{\bar{F}} \int_C \phi_e(x, y, t) dx, \quad (36)$$

where the subscripts on η and ϕ refer to mass source (ρ), x -direction body force (u), y -direction body force (v), and internal energy source (e) controls. The maximum and average values of $|\eta|$ are listed in table 2 for each control. We see that the peak η is 0.23, required by an optimized internal-energy control, with corresponding average 0.028. From the viewpoint of required power, the y -direction body-force control is the most efficient, with an average $|\eta_v| = 1.87 \times 10^{-5}$ and peak $|\eta_v| = 1.90 \times 10^{-4}$. Defining η based on the mean \bar{F} yields the same conclusions.

4.4.5 Control dimensionality

The 10^7 control parameters optimized are expected to be far more than is needed to represent an effective control. We can estimate the necessary dimensionality of the control

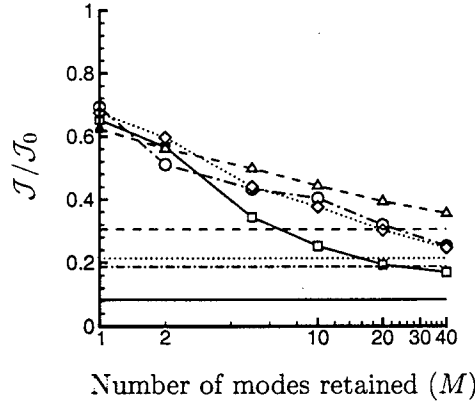


Figure 19: Sound reduction by controls rebuilt with the M lowest order modes: mass source \cdots , x -direction body-force $---$, y -direction body-force $- \cdot -$, and internal-energy $—$ controls. Horizontal lines show the full-mode limit. \mathcal{J}_0 is the uncontrolled \mathcal{J} .

by expanding it in empirical eigenfunctions. From a practical standpoint, the fewer modes needed and the more simple their form, the more likely effective active controls will be implementable. To obtain appropriate empirical eigenfunctions, we used the proper orthogonal decomposition,²⁹ also called the Karhunen–Loève decomposition. Specifically, the method of snapshots³⁰ was employed to provide a decomposition of the form

$$\phi(\mathbf{x}, t) = \sum_{i=1}^N a_i(t) \psi_i(\mathbf{x}), \quad (37)$$

where $\int \psi_i \psi_j d\mathbf{x} = \delta_{ij}$ and sums of the form $\sum_{i=1}^M a_i(t) \psi_i(\mathbf{x})$ for $M < N$ are optimal in the sense of representing the $\overline{\int \phi^2 d\mathbf{x}}$ energy. Figure 18 shows the eigenfunction mode energies of the optimized controls. Typically, 50% of the total control energy is in the first 10 modes, and 75% is in the first 20. Perfect pairing of the lower modes is seen for the x -direction body-force control, which we shall see in section 4.4.6 also appears to control the flow somewhat differently than the other controls.

Since these eigenfunctions merely provide a spectral representation of the data, with no direct link to control effectiveness, we must verify that a small number of these modes can indeed be successful. Controls ϕ^M reconstructed with only the M lowest-order modes were thus applied to the original flow. As shown in figure 19, the y -direction body-force control reconstructed with the first mode only, which captures 23% of the overall $\int \phi^2 d\mathbf{x}$ energy, reduces the cost \mathcal{J} by 38% (2.1 dB). With the second mode also included, the y -direction body-force control reduces the cost \mathcal{J} by about 44% (2.5 dB). This cost reduction is better as more modes are included. When 40 modes are included to rebuild the y -direction body-force control, the cost is reduced by 64% (4.4 dB), which is close to its full-mode limit 69% (5.1 dB). The noise reduction by internal energy source control rebuilt with 40 modes is 82% (7.4 dB), which is also close to its full-mode limit 92% (11 dB). Similar effectiveness is observed for all other types of control.

Though a small number of modes can be effective, their form is nontrivial. Figure 20 shows the first 4 empirical eigenfunction modes for the y -direction body-force control. The spatial scale appears to be smaller as the mode number increases. The corresponding time

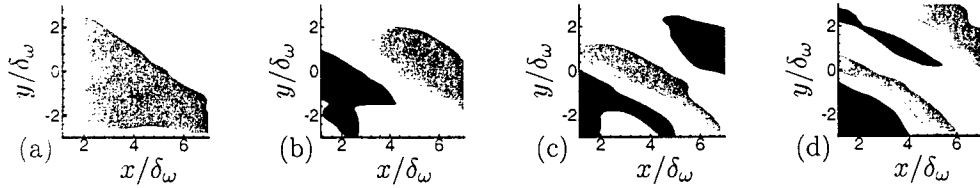


Figure 20: Spatial shape of the empirical eigenfunction basis for the control: (a) mode 1; (b) mode 2; (c) mode 3; and (d) mode 4. The black shows values lower than -0.15 , and the gray shows values higher than 0.15 .

coefficients $a_i(t)$ are reported elsewhere,¹⁷ and have as expected higher frequency content for higher modes. The spatial form of the control is also important. We attempted to control the noise with an *ad hoc* pre-specified spatial shape,

$$\phi(\mathbf{x}, t) = \hat{\phi}(t) \exp(\sigma_0 |\mathbf{x} - \mathbf{x}_0|^2), \quad (38)$$

with \mathbf{x}_0 the center of \mathcal{C} and $\sigma_0 = 0.1$. In this case, the optimized $\hat{\phi}(t)$ for the x -direction body-force control reduces the noise by 44%, but the other types of control achieved at most a 20% reduction.

4.4.6 Control induced changes to the flow

Having the original noisy flow and a perturbed version of it that is significantly quieter provides an opportunity to study the changes that make the flow quiet. The ‘before’ and ‘after’ flows are compared in the following sub-sections.

Energetic structures. Several studies of single-frequency or harmonically excited free shear flows^{9,16,27,31} suggest some connection between vortex pairing and sound radiation. However, for our randomly excited flow, our control reduces the noise substantially without suppressing pairing or substantially changing the vortex structure at all. In figure 21, visualizations compare the flow before control (figure 21 a) and after control (figures 21 b through e), showing little change in the vortical structure of the flow. We heuristically arranged the visualizations of the controlled cases in order of increasing difference from the uncontrolled case. The y -direction body-force control causes almost no noticeable change: figure 21 (b) is almost indistinguishable from the uncontrolled case in figure 21 (a). This is also the case that demanded the least control energy. However, the internal-energy control case in figure 21 (c), which required the most control energy, also appears almost unchanged, but since the control in this case does not directly affect the vorticity, its influence might be expected to be less apparent in this visualization. The mass-control case shown in figure 21 (d) is noticeably different, but the same pairings seem to occur at approximately the same locations. The x -direction body force in figure 21 (e) is the only case that appears to have any fundamental difference. These randomly excited flows can be contrasted to the highly organized harmonically excited flow in figure 21 (f).

To avoid any bias caused by only showing four closely spaced snapshots and to provide a more complete picture of the vortex evolution, in figure 22 we show the entire history of large structures as designated by the pressure fluctuations at $y = 0$. The convergence of low-pressure structures, the black branches in the figure, are an indication of vortex mergings. Again we see slight changes where vortices merge and so on, but the changes

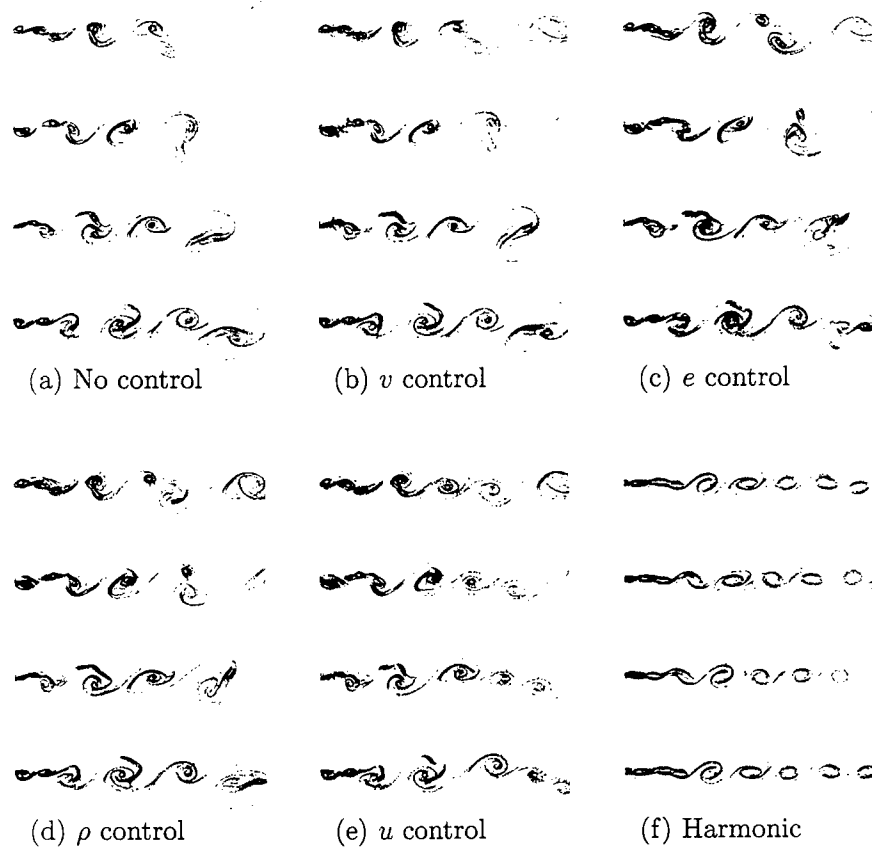


Figure 21: Instantaneous vorticity field visualizations at times $ta_{\infty}/\delta_{\omega} = 312.5, 331.0, 351.1$, and 371.3 , with contour levels from $-0.6\Delta U/\delta_{\omega}$ to $0.02\Delta U/\delta_{\omega}$: (a) no control; (b) y -direction body-force control; (c) internal energy source control; (d) mass control; (e) x -direction body-force control; and (f) the harmonically excited case, which is indistinguishable before and after control.

caused by even the x -direction body force in this more complete picture do not indicate any fundamental change, with most (though not all) of the low-pressure mergings occurring near to the locations they appear in the uncontrolled case. All these observations bring us to the conclusion that there is no fundamental relation between vortex pairing *per se* and the part of the noise reduced by our controls in the present mixing layers.

Mean-flow and fluctuation statistics. Given the qualitative similarity of the flow before and after the control is applied, one should not be surprised that the mean flow and turbulence statistics are also nearly unchanged. Figure 23 (a) shows that momentum thickness, defined by

$$\delta_m = \int_{y_a}^{y_b} \frac{\rho(u - U_a)(U_b - u)}{\rho_{\infty}\Delta U^2} dy, \quad (39)$$

is nearly linear in x and only slightly changed by any of the controls for all four cases, though they all suppress spreading slightly around $x = 60\delta_{\omega}$. In (39), U_a and U_b are the x -velocity at y_a and y_b and results were, of course, insensitive to the y_a and y_b .

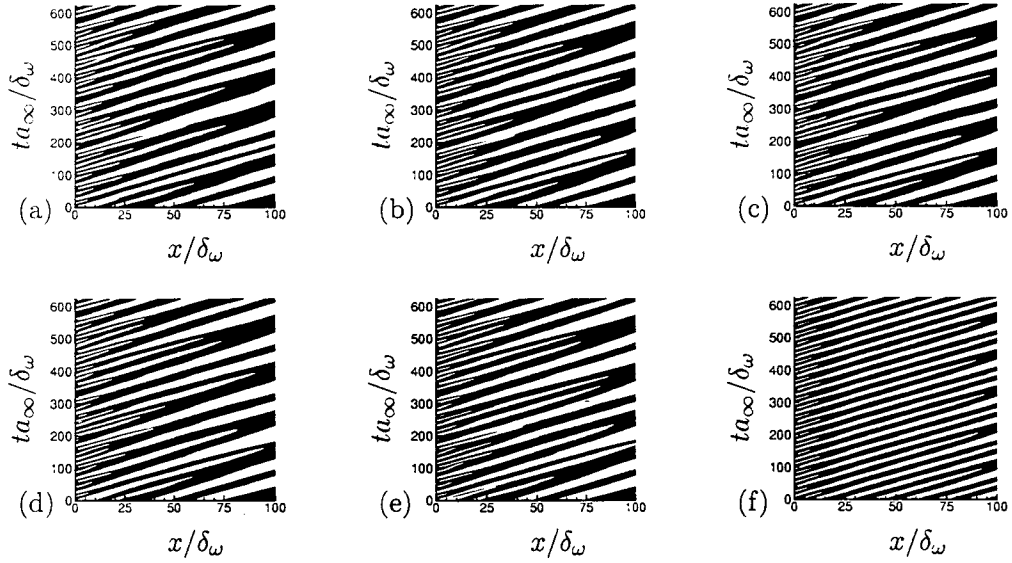


Figure 22: Pressure evolution at $y = 0$: (a) no control; (b) y -direction body-force control; (c) internal energy source control; (d) mass control; (e) x -direction body-force control; and the (f) harmonically excited case. Black is $(p - p_\infty) < 0$; white is $(p - p_\infty) > 0$.

Second-order statistics of the flow fluctuations are also nearly unchanged. With E_k defined in (32), the y -integrated mean fluctuation kinetic energy normalized by the local mean momentum thickness (39),

$$E_t(x) = \frac{\int_{-80\delta_\omega}^{80\delta_\omega} \overline{E_k} dy}{\delta_m(x)}, \quad (40)$$

is plotted in figure 23 (b). This quantity reaches its maximum near $x = 25\delta_\omega$ and remains constant downstream. The control was applied from $x = \delta_\omega$ to $x = 7\delta_\omega$, where the turbulence intensity is about 70% of its fully developed level, though the mixing layer is already spreading linearly at this point and at the same rate as for large x . Thus, the control was optimized and applied in a region where the unsteady flow fluctuations have amplitudes close to their nonlinearly saturated condition. Moving C further downstream to where the fluctuations are somewhat more intense and increasing its size in proportion to the local momentum thickness showed similar success. The small effect of the control on the flow is clear in that the turbulence kinetic energy has not been changed much by the controls. The noise control is not by a suppression of the unsteady fluctuations.

Evolution of the energetic flow structures. Based on these results, it is clear that subtle aspects of the manner in which the fluctuation energy is arranged in the flow must be responsible for the noise reduction we observe. Assuming for discussion the simplest description of sound source and propagation discussed in section 4.1, it is potentially subtle aspects of their evolution as they advect downstream that puts energy into components with supersonic phase velocity in x , which can then radiate to the far field in y . The specific interactions that disrupt smooth advection in x are, however, difficult to quantify. Interactions with a short length scale in x , or similarly on a short time scale, will broaden the corresponding Fourier transforms in k and ω and thus potentially increase energy in

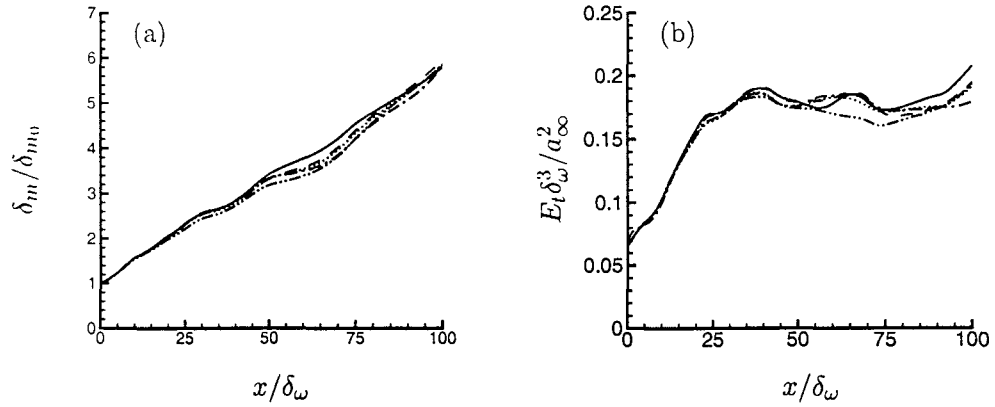


Figure 23: (a) Momentum thickness (39) of the mean flow (normalized by δ_{m0} , the initial momentum thickness at $x = 0$). (b) Fluctuation kinetic energy integrated in y (40) direction. Lines in both figures show cases without control —; and with mass source control, x -direction body force - - - -, y -direction body force - - - -, and internal energy source - - - - controls.

components that can radiate. However, analysis of direct numerical simulation data suggests that all Fourier modes participate in the interaction.³²

Here we seek a means of assessing how smoothly the flow's energy advects downstream. For convecting structures in a quiet streamwise homogeneous flow, we would expect to find that the flow's fluctuations would be representable by Fourier modes with only subsonic (or mostly subsonic) phase velocities. A way for them to be quiet would be for them to advect nearly unchanged, which would give them a form such as $a_1(t) \cos kx + a_2(t) \sin kx$, with $a_1(t)$ and $a_2(t)$ tracing circles in their phase plane. In the present streamwise inhomogeneous case, Fourier transforms are clumsy.³ Though they do provide a definitive partitioning of the energy into radiating and non-radiating components, their physical interpretation is clouded by the fact that individual k - ω modes may extend beyond the length of the physical flow. Therefore, we employ empirical eigenfunctions in the inhomogeneous-flow x direction to assess the advection of energy. The proper orthogonal decomposition is again used here to provide empirical basis functions as it has been used in numerical and experimental efforts in designating flow structures in jets.³³⁻³⁵ We define the empirical eigenfunctions by a kinetic energy norm

$$\|\mathbf{q}\|^2 = \int_{D_p} (u^2 + v^2) dx, \quad (41)$$

where D_p is the entire physical domain in our computation, and can then reconstruct the flow by

$$\mathbf{q}(\mathbf{x}, t) = \sum_{i=1}^N a_i(t) \psi_i(\mathbf{x}). \quad (42)$$

Taking the harmonically excited mixing layer as an example, we see that the kinetic energy of the two most energetic modes is nearly the same (figure 24 a), the corresponding modes fit together as sines and cosines (figure 24 b), and their time coefficients trace circular trajectories in their phase plane (figure 24 c). This is the type of behavior we anticipated for this quiet flow. Remarkably, we can observe a switch to this type of underlying behavior with the application of our control even in the randomly excited flow.

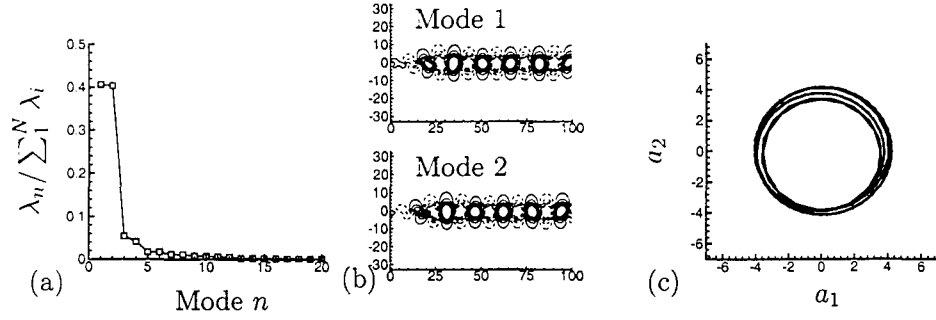


Figure 24: The empirical eigenmodes of the harmonically excited mixing layer: (a) relative mode energy as in figure 18; (b) the pv component of modes 1 and 2 with — showing positive and ---- showing negative contours; and (c) the phase plane of the coefficients of modes 1 and 2.

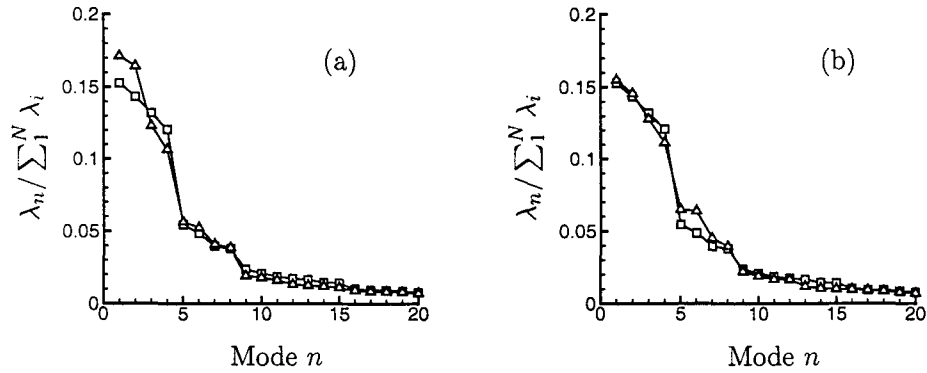


Figure 25: Relative energy of represented by the lowest-order empirical eigenfunctions before \square and after \triangle control: (a) y -direction body-force and (b) x -direction body-force controls.

We focus the y -direction body-force control case for discussion, but the results are general. Figure 25 (a) shows the relative energy represented by each eigenfunction before and after the y -direction body-force control is applied. While they are similar before and after, it is noteworthy that mode energy levels come more closely in pairs up through mode eight. The eigenfunctions also pair up. Figure 26 shows the y -momentum components of the vector-valued eigenmodes. After control, they come more closely in out-of-phase pairs, like sines and cosines. Further, and perhaps more importantly, their time-dependent coefficients now give their net behavior a smoother downstream traveling character. Figure 27 shows the coefficients $a_1(t)$ and $a_2(t)$ of the first two modes before and after the control is applied. The x -momentum components of the eigenmodes show similar behavior.

The cases using mass control and internal energy control show very similar behavior to that discussed above for the y -direction body force control. However, for the x -direction body-force control, the energy of each mode is paired up differently (see figure 25 b). It seems to couple the 5th and 6th eigenmodes of the flow. For the y -direction momentum components of the modes (see figure 28 a and b), a coupling into sine- and cosine-like modes occurs for modes 5 and 6. Correspondingly, the phase picture of the coefficients $a_5(t)$ and $a_6(t)$ also shows more circular motion compared with the original flow (figures 28 c and d). We saw in figure 15 that this control is more successful at higher frequencies than the y -body-force control.

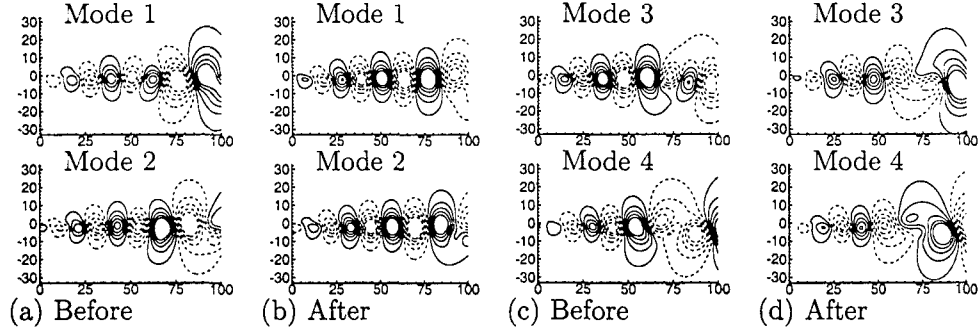


Figure 26: The ρv component of the four most energetic empirical eigenfunction modes before and after y -direction body-force control with — contours showing positive levels ≤ 0.03 and ---- contours showing negative levels ≥ -0.03 .

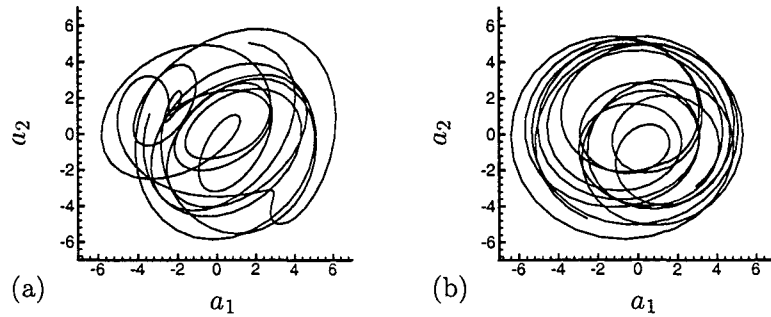


Figure 27: Phase map of the coefficients of the first 2 empirical eigenfunctions (a) before and (b) after y -direction body-force control.

4.5 Discussion and Conclusions

In summary, the adjoint-based optimal control framework that we formulated and implemented was able to circumvent the complexity of the flow's interactions leading to noise generation and significantly reduce it directly. It “chose” to do this by subtly changing the evolution of the existing turbulence structures in the flow. Only slight changes in the loca-

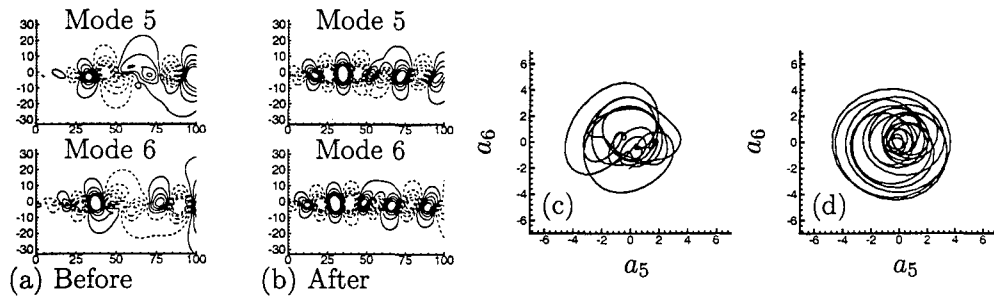


Figure 28: Plots (a) and (b) show the ρv component of modes 5 and 6 before and after x -direction body-force control with — contours showing positive levels ≤ 0.03 and ---- contours showing negative levels ≥ -0.03 . Also shown are the phase maps of the coefficients of the these modes before (c) and after (d) x -direction body-force control.

tions of pairing and other identifiable events were noted and the turbulence statistics were nearly unchanged by the control. Since essentially the same vortex pairings were observed before and after the application of the control, we conclude that it is not pairings *per se* or any other clearly identifiable near-field flow mechanics that are responsible for making a considerable fraction of the total noise.

The clearest picture of the changes to the flow came from decomposing it into empirical eigenfunctions, which show that the controlled turbulence structures advect more uniformly downstream. The eigenfunctions of the controlled flow come in sin-cos like pairs, with coefficients that trace relatively circular trajectories in their respective phase planes. This interpretation was reinforced by results for a harmonically (as opposed to randomly) excited mixing layer. In this case the control was ineffective, but the flow was already acoustically inefficient, radiating comparably to the controlled randomly excited cases. The empirical eigenfunctions also shared key features with the randomly excited but controlled flow. They came, as expected, in distinct sin-cos pairs whose coefficients traced near perfect circles in their corresponding phase plane.

It has long been understood that the largest turbulent flow structures in inflectional free shear flow bear considerable resemblance to the linear instability modes supported by the same flow. This is especially true in two dimensional flow, which lacks the vortex stretching mechanism for removing energy from these structures via the turbulence energy cascade. Such similarity has inspired several efforts to model aspects of free-shear-flow noise using wave-packet models for the noise sources. These have included attempts based on both actual linear instability modes^{8,12} and relatively *ad hoc* wave packets, which match the qualitative character of growing then decaying instability modes.^{9,10} Collectively, these have met with some success, often predicting aspects (*e.g.* functional forms) of observed experimental results but typically are not complete, predicting for example erroneous angles of silence.^{8,12} A factor contributing to this difficulty is the remarkable sensitivity of sources of this form to perturbations, which presumably occur due to nonlinearity in any nonlinearly active free shear flow, making it louder. One can speculate that a free shear flow, at least a relatively simple two-dimensional one, is in some sense near an acoustically less efficient unperturbed wave-packet state. Based upon the results presented in section 4.4.6, such an acoustically inefficient state has been found by our control. Supporting this view, the angles of silence observed for narrow frequency bands (figure 15) are similar to those predicted by some wave-packet-based models. Three-dimensional turbulent flows are also known to have an underlying instability wave-like character, but it remains to be seen if they can be perturbed into a quieter state as easily as the present two-dimensional flow.

Though we have optimized the control, no conclusions can be made about whether or not this control is truly optimal and does not just represent a local minimum. It is possible that a quieter flow might be achieved by starting from a different ϕ point. A laminar flow would be an obvious target state, but what specific control could achieve this in a free shear flow is unclear when the slightest disturbance will once again seed instability growth and eventual nonlinear development in the flow. In contrast, the optimized control we found appears to be a stable local minimum. Regardless, laminarization is probably not a possibility for the selected C because it does not extend entirely across the thickness of the mixing layers.

From a practical perspective, an attractive feature of the identified control is that it is a relatively minor perturbation to the flow that does not change the fundamental hydrodynamics,

though it remains unclear how one might find such a controller in practice. Unfortunately, the control itself was also complex, defying any clear interpretation. Based on space-time correlations, it was seen to advect in its region of support at the same speed as the local flow structures. A decomposition into empirical eigenfunctions showed that controls reconstructed with only one or two modes, which capture only 20 to 30% of the energy, achieved 40 to 50% sound reduction. Optimizing only the time coefficient of a Gaussian-pulse-shaped actuation reduced the noise up to 44%, but was only this successful for the x -direction body-force control.

5 Three-dimensional Mixing Layer

The tools have been developed and demonstrated for application of optimal controls to study the noise mechanisms of two-dimensional mixing layers. Using them to study the “real” three-dimensional case is now important for two main reasons. First, while it is known that the underlying structure of three-dimensional shear layers, which make up the near nozzle region of a turbulent jet, are essentially two-dimensional, their dynamics are much more chaotic. Streamwise correlation lengths are shorter, which will potentially inhibit the effectiveness of the control.

Second, the radiated sound spectra of three-dimensional turbulent flows are much broader banded than their two-dimensional counterparts. In engineering applications, the higher frequencies they include are particularly important because they receive a large weighting when accounting for human annoyance.

We expect the task of creating optimal noise reduction controls will be significantly more difficult in three dimensions. This is due in part by the above mentioned characteristics of the flow, and increased computational challenges. The automatic optimization process will now have to be used to its fullest capacity to make any control realizable.

5.1 Numerical Methods

For this three-dimensional mixing layer, the notation for the governing flow equations in section 4.2.2 is the same with the addition of the added terms in $\mathcal{N}(\mathbf{q})$ due to the third dimension (see Appendix A). The specific \mathbf{F} vectors found in table 1 are also trivially changed. As for the control formulations, sensitivity, and adjoint formulations found in sections 4.3.1, 4.3.2, and 4.3.3, the method does not deviate and the adjoint equations in three dimensions can be found in Appendix C.

5.1.1 Flow parameters and domain

The three-dimensional mixing layer simulated is shown in figure 29. The velocity difference across the mixing layer is again ΔU and the inflow momentum thickness is defined exactly as in equation 2. The mach numbers of the free streams are $M_1 = 0.9$ and $M_2 = 0.0$ based on the ambient sound speed a_∞ . The flow was nondimensionalized via a_∞ , the inflow momentum thickness δ_w , and the ambient density ρ_∞ . The density and viscosity were the same in both streams and zero bulk viscosity was assumed. The Reynolds number was 200 based on this nondimensionalization and the Prandtl number was 0.7.

The physical domain of the simulation extended to $75\delta_w$ in the streamwise direction (x), to $12.8\delta_w$ in the spanwise (z), and from $-80\delta_w$ to $12\delta_w$ in the cross-stream (y). The control

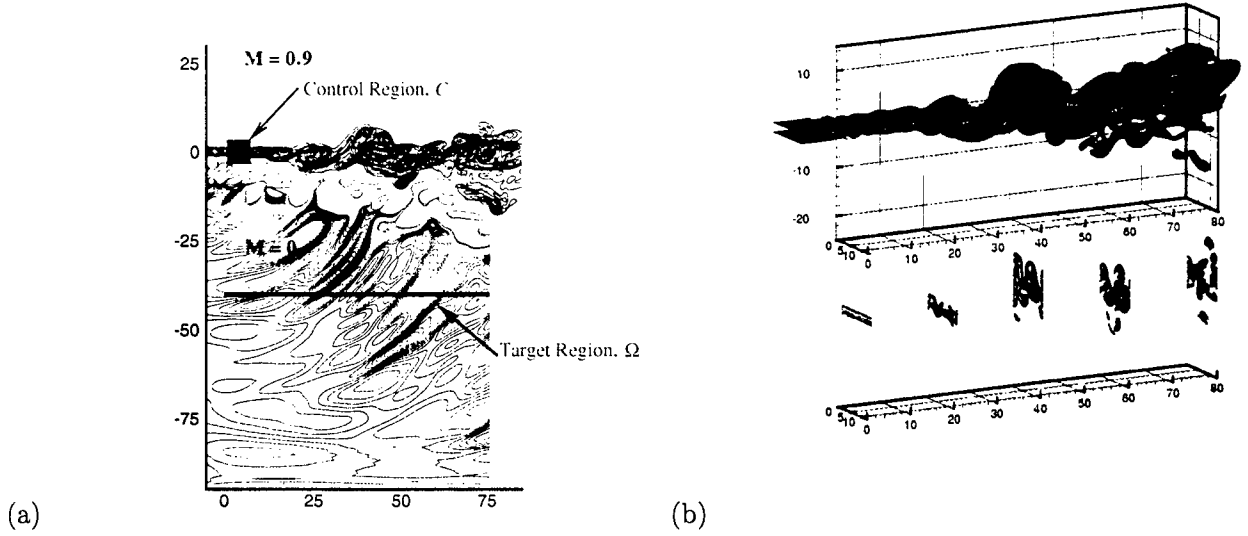


Figure 29: (a) Dilatation and vorticity magnitude fields for the three-dimensional mixing layer. (b) Isosurfaces of vorticity (top) and vorticity slices corresponding to various x locations (bottom).

region \mathcal{C} extended from $x = [0, 7]$, $y = [-4, 4]$, and $z = [0, 12.8]$ and had a mesh of $39 \times 53 \times 48$ in those respective directions. The target region (now an x - z plane) was located at $y = -40$ and was the same in the streamwise and spanwise directions as the physical domain. It had a mesh of 442×48 points. For comparison of the effectiveness of the control, the simulation also tabulated values of the cost function on a plane located at $y = -75$.

5.1.2 Spatial discretization and time advancement

Grid stretching was used in both the streamwise and cross-stream directions to increase resolution in the shear layer. The grid was uniform in the spanwise direction, which was periodic.

The stretching of the grid was obtained by mapping the computational mesh on to a uniform mesh via a function $x = g(s)$. Using a mapping such as this, derivatives of a function $f(x)$ are related to derivatives on the uniform grid by:

$$\frac{\partial f}{\partial x} = \frac{1}{g'} \frac{\partial f}{\partial s} \quad \text{and} \quad \frac{\partial^2 f}{\partial x^2} = \frac{1}{g'^2} \frac{\partial^2 f}{\partial s^2} + \frac{g''}{g'^3} \frac{\partial f}{\partial s} \quad (43)$$

where primes indicate differentiation by the parameter s .

In practice, it is simpler to specify the form of $g'(s)$ since it is directly proportional to the grid spacing. For all simulations, the form was specified using combinations of hyperbolic tangent functions:

$$g'(s) = \frac{L_{\max}}{g_0} \left[1 + \frac{\alpha_1}{2} (1 + \tanh[\sigma_1(s-1)]) + \frac{\alpha_2}{2} (1 + \tanh[\sigma_2 s]) \right] \quad (44)$$

The constant g_0 was set such that $g(1) = L_{\max}$ and so the uniform grid extends from $s = 0$ to $s = 1$. Integration and differentiation with respect to s yield g and g'' , respectively,

Spatial Domain Parameters							Grid Stretching Quantities			
	$N_{x,y,z}$	L_{\max}	α_1	α_2	σ_1	σ_2		\mathcal{D}_{\max}	\mathcal{D}_{\min}	Max Stretch %
x	512	125	50	9	60	50	x	4.315	0.152	3.1%
y	400	125	8.5	10	12	3.7	y	0.858	0.175	18.7%
z	48	12.8	–	–	–	–	z	0.267	0.267	–

Table 3: Parameters used in Eqs. 44 & 45 for the discretization and grid stretching in the simulation.

which allow for derivative calculations using Eq. 43. The grid in the spanwise direction was divided into N_z evenly spaced intervals with spacing

$$\mathcal{D}z = \frac{L_{\max}}{N_z - 1} \quad (45)$$

where N_z is the number of grid points in the z direction.

The quantities used for the parameters L_{\max} , α_1 , α_2 , σ_1 , and σ_2 are shown in Table 3. Also shown are the maximum and minimum grid spacings, \mathcal{D}_{\max} and \mathcal{D}_{\min} and amount of grid stretching for the parameters chosen. The maximum stretching and spacing occurred on the computational domain boundary. The minima were found in the shear layer.

The time advancement scheme for the three-dimensional flow and adjoint simulation used was the High-Accuracy Large-Step Explicit Runge-Kutta (HALE-RK) developed with problems in computational aeroacoustics in mind.³⁶ The HALE-RK7 (seven step) scheme was used for this simulation since the CFL stability limit was doubled and the CFL accuracy limit increased by 60% over the traditional Runge-Kutta (four step) fourth-order scheme. This allowed for the time step of the simulation to be more than doubled to $\Delta t = 0.125\delta_\omega/a_\infty$ (where it would be limited to $0.06\delta_\omega/a_\infty$ before) with no losses in accuracy or stability. Furthermore, with this larger time step, the optimization time horizon could be doubled at less cost, giving the control greater authority to make noise reducing changes to the flow.

5.1.3 Differencing schemes

The methods of calculating derivatives used here were chosen to reduce the number of mesh points as much as possible to lessen computational constraints. The cost associated with greater accuracy in differencing schemes, despite requiring larger stencils and more parallel communication, was acceptable since higher-accuracy schemes required less points per wavelength to resolve wavenumbers characteristic in the flow. Both explicit and implicit schemes which traded formal accuracy order for enhanced dispersion qualities were used.

An implicit “spectral-like pentadiagonal” differencing scheme²¹ was used in the cross-stream direction. This scheme enhanced resolution compared to the eighth- and tenth-order schemes that share the same differencing stencil with a formal fourth-order truncation error. The coefficients are formed by ensuring exactness of the modified wavenumber at three anchor points, $k = [2.0, 2.3, 2.4]$ such that $k'(k) = k$ at those points. These constraints sacrifice the formal order of the scheme in return for lessened dispersion error. The left of figure 30 shows the modified wavenumber ($k'(kh)$, where h is the grid spacing) for this scheme. Also shown are the tenth-order compact finite difference scheme given by Lele²¹ and the sixth-order scheme developed by Lui and Lele³⁷ for comparison.

An error metric denoting the deviation of the scheme from the exact wavenumber is shown on the right in figure 30. The relative error as a function of wavenumber, $\epsilon(k)$ is defined as:

$$\epsilon(k) = \frac{k'(k) - k}{k} \quad (46)$$

In the streamwise direction a variant of the explicit dispersion-relation-preserving or DRP²² scheme was used. In the original fourth-order scheme, the coefficients of a seven-point stencil were optimized in order to minimize $\epsilon(k)$ on the interval $kh = [0, \pi/2]$. The scheme developed for this simulation used a nine-point stencil and minimized the error on $kh = [0, 7\pi/12]$. The resulting scheme is sixth-order accurate and is shown along with the original in figure 30. An explicit scheme was chosen in the streamwise direction to facilitate domain decomposition for parallel computing in that direction.

5.1.4 Inflow turbulence procedure

For our previous two-dimensional mixing layer simulations, we specified an *ad hoc* sum of randomly phased modes (see section 4.2.4). To properly challenge the controller and provide more realistic turbulent inflow conditions we have created a means to “feed” developed turbulence from an auxiliary simulation into the mixing layer simulation. This is shown schematically in figure 31. Subsequent x - z planes from the “frozen” streamwise periodic auxiliary simulation of a temporally developing mixing layer are used as the target state of a buffer zone at the inflow. In this buffer zone, the flow equations (equation 3) are modified to be

$$\mathcal{N}(\mathbf{q}) + \sigma(x)(\mathbf{q} - \mathbf{q}_{\text{target}}) = 0. \quad (47)$$

The extra term in this expression “damps” the solution toward the target state, in this case the appropriate inflow conditions. The feeding coefficient, σ , determines the domain over which the target state is forced and has the form

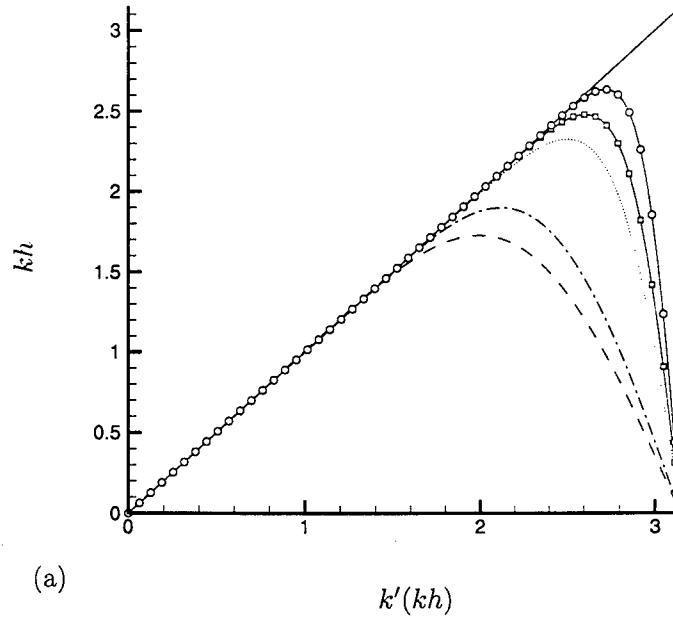
$$\sigma(x) = \frac{1}{2} \left(\tanh \left[\frac{1}{\sigma_f} (x - x_l - x_r - x_b) \right] - \tanh \left[\frac{1}{\sigma_f} (x - x_l + x_b) \right] \right) \quad (48)$$

where x_l and x_r form the left and right edges of the feeding domain and σ_f and x_b are parameters which smooth the function.

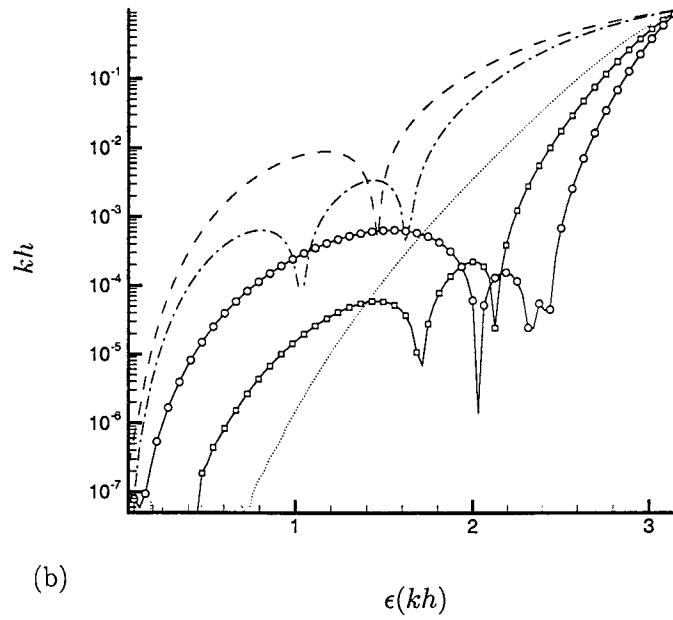
New data is fed from the auxiliary simulation at the estimated convection speed $U_c = (U_1 + U_2)/2$, which is the mean speed of the two streams. The x -domain of the auxiliary simulation is periodic, so the inflow data will repeat eventually, but the period of this data is long enough to allow two flow through times before a repeat. This is longer than the time required to properly evaluate the controls and their effect on the noise mechanism in the three-dimensional mixing layer.

5.1.5 Boundary treatments

A buffer region was used in the simulation to mimic a radiation condition in a manner similar to that proposed by Freund²³ (see equation 5). The dampening coefficient ξ was varied from 0 to 0.4 in the streamwise direction and from 0 to 0.6 in the cross-stream direction. The buffer region extended $15\delta_\omega$ to the left of the physical domain and $30\delta_\omega$ to the right. The cross-stream buffer and $12\delta_\omega$ beyond the top and bottom of the physical domain. The spanwise direction was periodic and therefore required no boundary condition.



(a)



(b)

Figure 30: (a) Plot of the modified wavenumber of the first derivative schemes used in this simulation. (b) Error in the first derivative schemes. — Exact (Spectral) differentiation, ---- DRP (4th Order), -.-.- DRP (4th Order), Compact 10th Order Scheme, -□- Lui (6th Order), -○- "Spectral-like Pentadiagonal"

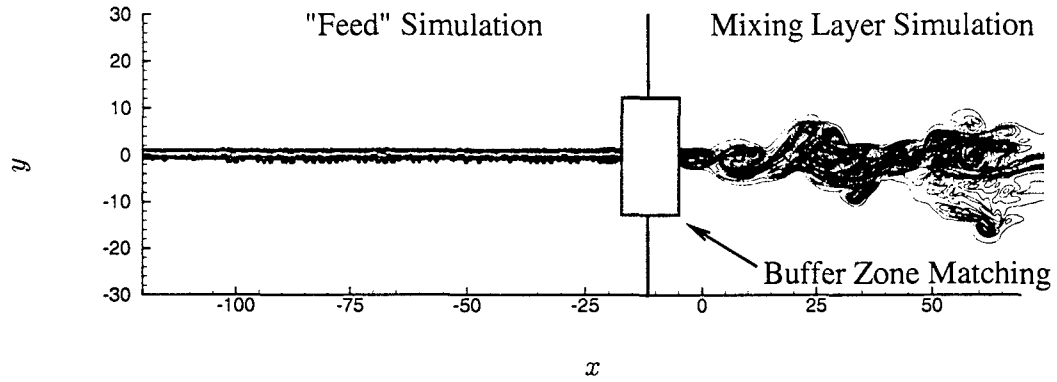


Figure 31: View of the auxiliary simulation data (shown here as vorticity magnitude) as it is fed into the mixing layer. The buffer region extends from $-15 < x < -5$.

During the course of testing the code for the adjoint simulation, it was found that large amplitude disturbances were excited as they interacted in the shear layer. Since the equations are solved backwards in time, these disturbances traveled upstream and into the left buffer region, which is weakly dampened due to the fact that the flow solution travels in the opposite direction. Therefore, the coefficient ξ was quadrupled in the area upstream of the control region \mathcal{C} to dampen the waves before they reached the computational boundary.

As mentioned in section 4.2.3, standard one-dimensional characteristic boundary conditions were used for both the adjoint and flow fields to absorb outgoing perturbations.

5.1.6 Simulation procedure

The flow was started from an initial velocity profile of

$$u(x, y) = \frac{1}{2} M_1 \left(\tanh \left[20.5 \frac{y}{x} \right] + 1 \right) \quad (49)$$

with $\rho = 1$, $p = 1/\gamma$ and zero cross-stream and spanwise velocities. The inflow turbulence was fed and the flow was simulated for 3700 time steps ($449\delta_\omega/a_\infty$). This allowed for all transients to disappear before accumulating statistics or applying the control. The flow also was at a point where a statistically stationary time series could now be computed for determining the quality of the turbulence.

The control time horizon was 5000 time steps, or a time of $625\delta_\omega/a_\infty$. This allowed for the following process to occur five times: the effect of control ϕ is advected from the region \mathcal{C} at speed $U_c = 0.45$ to a mid-point in the shear layer and subsequently generates a sound event which travels at speed $a_\infty = 1$ to the target plane Ω . This time ensures that the control not only reaches the target plane, but has ample opportunity to reduce noise there. The number of control parameters for this optimization procedure is 500 million.

5.1.7 Three-dimensional adjoint and control considerations

For this simulation, several features of the numerical implementation needed to be changed from the previous two-dimensional framework due to (1) the inclusion of the third dimension, and (2) the greater computational burden associated with this addition.

First, the δ -function distribution shown in equation 26 must now approximate the smearing on to an x - z plane. This was achieved with the same Gaussian-shaped function listed in section 4.3.4 for the cross-stream direction. A combination of hyperbolic tangents functions similar to equation 48 smeared the streamwise direction between its ends at $x = [0, 75]\delta_\omega$. The spanwise direction was periodic, so no smearing was required.

Since the entire flow field needed to be saved to solve the adjoint equations, every other point in the x - and y -directions was stored. A FFT was taken in the z -direction and half of the lowest (and most energetic) Fourier coefficients were retained. This data was written to disk every ten time steps throughout the simulation. The data was again interpolated linearly in time and used second-order Lagrange interpolation in space for the x - and y -directions. An inverse FFT using the stored coefficients finished recreating the flow field.

This process amounted to a large computational savings in I/O operations and disk space. The two-dimensional simulation was able to save the entire flow field within the memory. However, the problem size of this simulation was too large to reside in memory and therefore had to be distributed across multiple nodes when the data was written to disk. This data sharing was used for the flow field coefficients and for the conjugate gradient portion of the code. Several gradients and controls needed to be stored since the control algorithm produced gradient directions that were conjugate to all previous gradients.

The control update process exhibited similar behavior to the previous simulation. The number of flow and adjoint solutions computed per line minimization was comparable, but slightly higher, due to differing local shapes of $\mathcal{J}(\phi)$.

5.2 Basic flow results

5.2.1 Visualization

Figure 29(b) in addition to figure 32 show the three-dimensional structure of the flow and its fundamental differences from the two-dimensional simulation. The vortex stretching mechanism creates a much more chaotic flow even at a lower Reynolds number. The left of figure 32 shows a visualization as a x - y slice taken through the mid-plane of the spanwise direction of the simulation of the mixing layer. Contours of the magnitude of vorticity in the shear layer and contours of the dilatation are shown. The dilatation is proportional to the time derivative of the density, via $n_1(\mathbf{q})$ in (55) far from the mixing layer. Here the speed of sound is constant and the density is proportional to the pressure though $p = a_\infty^2 \rho$.

Figure 32(b) shows the much broader far-field sound spectrum of the mixing layer. Pressure data was taken at midpoints in the spanwise and streamwise directions and at $y = -75$ for all 5000 time steps in the simulation. A windowing scheme³ modified the time series data due to its finite nature to confine spurious spectral aliasing to very low wavenumbers.

A slice at the midpoint in the spanwise direction of the adjoint pressure field is shown in figure 33. As before, the adjoint pressure begins as a sound wave forced by the flow data on the Ω -plane and travels upstream to excite disturbances in the shear layer.

5.2.2 Mean and turbulence statistics

Data from the simulation was output every 10 time steps ($1.25\delta_\omega/a_\infty$) and used to compute statistical turbulence quantities. The mean, Reynolds stresses, and similarity features of

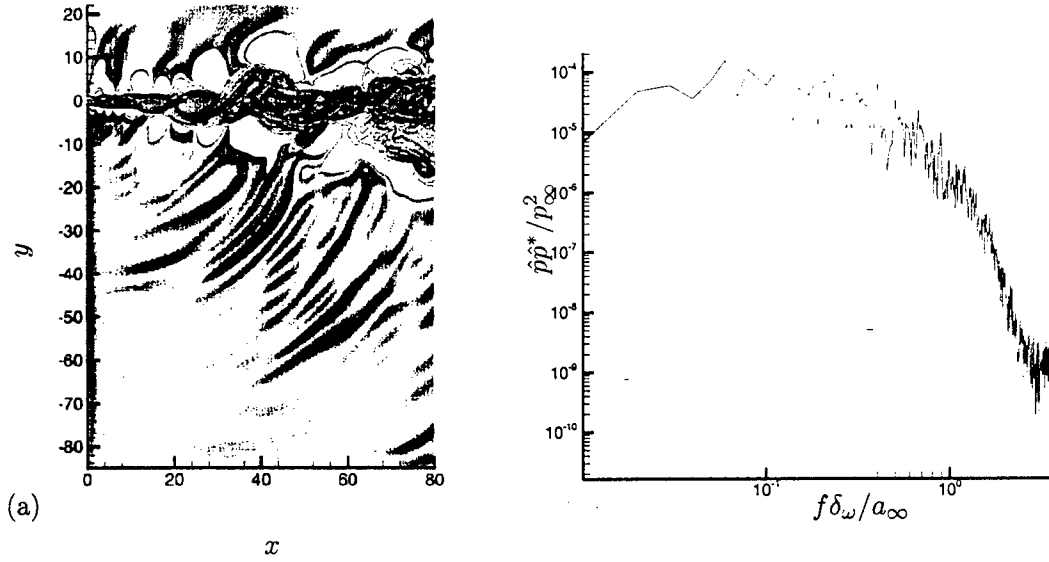


Figure 32: Visualization of the three-dimensional mixing layer vorticity and dilatation (left) and the far-field sound spectrum (right).

the flow were calculated using 501 data files. This is not a large sample and the statistical quantities reported may not be fully converged. However, the results presented suggest that the turbulence is rich and capable of being realistic.

The mean quantities of the flow were calculated using Favre averaging. This is a common method for compressible turbulent flows where significant density fluctuation occur. Using the standard Reynolds averaging common in incompressible flow leads to a term in the continuity equation known as the turbulent mass flux which does not have a counterpart in the laminar equations. Therefore, under Reynolds averaging the Navier-Stokes equations require closure assumptions. Favre averaging uses a weighted density and a Favre-averaged quantity is defined by

$$\tilde{f} = \frac{\overline{\rho f}}{\bar{\rho}} \quad (50)$$

and the Favre decomposition of a flow variable is

$$f = \tilde{f} + f'' \quad (51)$$

The left of figure 34 shows the total mean kinetic energy of the mixing layer which is

$$K(x, y) = \overline{\rho u''u''} + \overline{\rho v''v''} + \overline{\rho w''w''}. \quad (52)$$

The figure shows that the mixing layer reaches its maximum mean kinetic energy near $x = 40$. The straight diverging contours suggest that the layer is growing linearly in the streamwise direction.

Figure 34 shows the self-similarity characteristics of the simulated mixing layer. The mean kinetic energy suggests that similarity occurs near $x = 40$. Shown with lines in figure 34(b) is the scaled $\overline{\rho u''u''}$ component of the Reynolds stress tensor (R_{11}) and with symbols, the

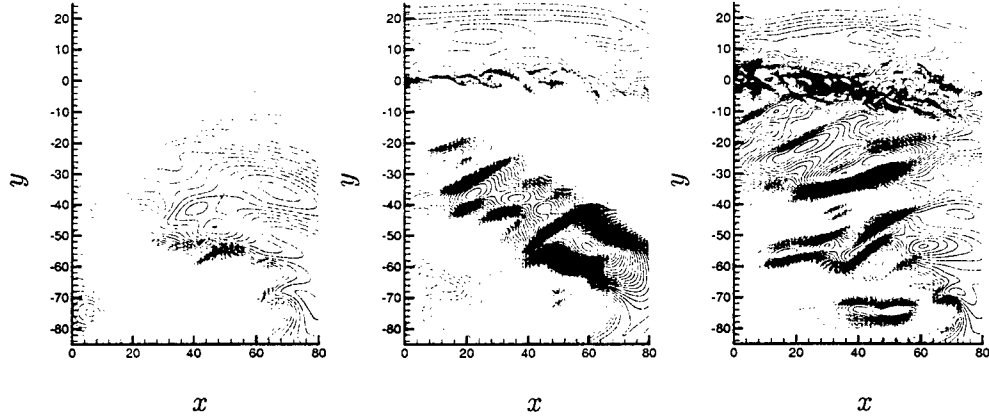


Figure 33: Snapshots of one plane of the adjoint pressure fields being forced in the target region Ω corresponding to the $y-z$ plane at $y = -75$. Time is progressing backwards from left to right.

$\widetilde{\overline{\rho u''v''}}$ component (R_{12}). The Reynolds stresses are scaled by ξ , a parameter scaled by the mixing layer thickness. The R_{11} and R_{12} components are shown at three downstream locations: $x = 55$, $x = 60$, and at the end of the physical domain at $x = 75$. To be perfectly similar, the profiles should collapse. Due to the small sample size, the peaks do not perfectly coincide, but it is apparent that the mixing layer reaches a self-similar state midway through its physical domain. The values for the scaled stresses and spreading parameters match well to comparable incompressible and compressible mixing layer simulations and experiments.

5.3 Preliminary optimization results

Having verified that the mixing layer was indeed a realistic turbulent flow, the internal energy control formulation was implemented. Since the flow is expected to be harder to control, the energy was chosen over the mass and body force controls solely due to its previous successes.

As of the writing of this report, the three-dimensional optimization has progressed to the fifth iteration. The computation was performed on an IBM P655 Power4+ system on 64 processors and required approximately 75 000 processor-hours and 1.2TB of disk space.

Initial simulations placed the target plane Ω at $y = -75$. Since the target region was far away, the control had to travel farther to make changes on the target line. So, the Ω -plane was moved to $y = -40$ (as shown in figure 29), which was found to be in the far-field, away from any significant nonlinear and viscous effects. This plane was determined by subtracting the contribution of the linearized Euler equations from the full Navier-Stokes solutions. A residual was calculated via

$$\mathcal{R}(x, y) = \int_0^{L_z} \int_0^T \sum_{i=1}^4 [\mathcal{N}_i(\mathbf{q}) - \mathcal{L}_i(\mathbf{q})]^2 dt dz, \quad (53)$$

where \mathcal{N} is the Navier-Stokes operator and \mathcal{L} is the linearized Euler operator. Figure 35 shows the residual plotted at several downstream locations. The residual drops steeply away from the shear region as expected. The line in figure 35 shows a decay to the fourth power. This represents the quadratic quadrupole decay (since the residual was a squared quantity,

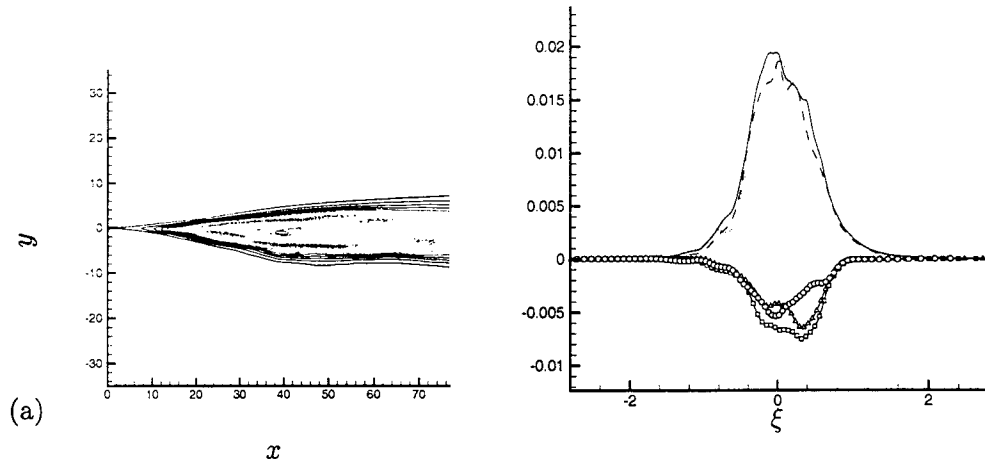


Figure 34: (a) Contours of the total mean kinetic energy. The contour space is 2.5×10^{-5} and the minimum and maximum levels are 3.5×10^{-5} and 6.8×10^{-4} , respectively. Right: Scaled Reynolds stress profiles in the mixing layer at various downstream locations. — $x = 55$ R_{11} ; ---- $x = 60$ R_{11} ; $x = 75$ R_{11} ; --□-- $x = 55$ R_{12} ; --△-- $x = 60$ R_{12} ; and --○-- $x = 75$ R_{12} .

the decay is doubled).

5.3.1 Cost reduction

Figure 35 shows the reduction of the cost function in equation 9 through the first five global iterations. The total overall noise reduction on the Ω -plane is 28%. As with the two-dimensional simulation, this plot featured a different starting point of the control time horizon. The starting point t_0 was increased to account for the uncontrollable noise on Ω due to the acoustic travel time of ϕ from \mathcal{C} . This decreased the cost function by roughly 35% of its original value.

Figure 36 shows this effect. The value of \mathcal{J} is shown with no control applied and after the fifth iteration. It is evident that there is no distinguishable difference between the values of the cost function until $ta_\infty/\delta_\omega = 600$ or for about one-fourth of the simulation's time series. Even at this point, it is likely that the control is not fully able to reduce noise on the target plane due to its width and the fact that changes due to the control may be advected by structures traveling at U_c and then emitted to Ω , a process which takes longer to occur.

Figure 37 compares x - y slices of the dilatation fields of the mixing layer far-field at $ta_\infty/\delta_\omega = 831.38$ with no control and with the control of the fifth iteration. Considering this qualitative view with the cost function in figure 36, it appears that the control is partially successful at reducing noise in the half-plane closer to \mathcal{C} in the streamwise sense. Many of the large sound events found in \mathcal{J} correspond to sound waves near the edges of the domain, that may not be as controllable as those more directly underneath where the control is applied.

The comparison of the two views of the shear layer also appears to agree with the previous simulation's results. The large structures appear to be changed, but not to a large degree. Noticable differences exist, but the sound field instead proves to be changed more radically. Although the noise has only been reduced 28% over the whole horizon, the higher amplitude

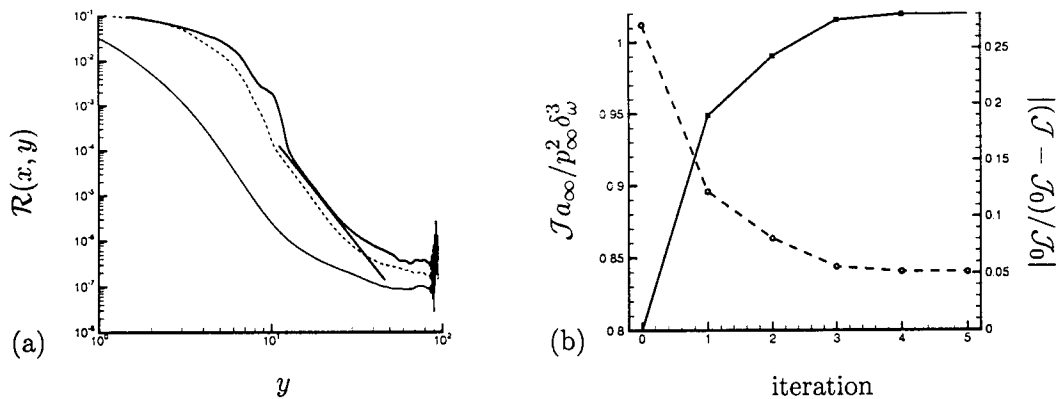


Figure 35: (a) The residual of the linearized Euler equations at — $x = 9$, ---- $x = 36$, and $x = 52$. The residual has been normalized by the maximum value. (b) Cost and — reduction due to the internal energy control after five iterations. J_0 is the original cost on Ω with no applied control.

events in the dilatation field are diminished.

5.4 Conclusions

It is partially evident, up to this point, that the controllability of the three-dimensional mixing layer provides somewhat more of a challenge than the previous simulation. If not merely in terms of computation, but also the ability to control the noise generation processes of an overall more chaotic flow regime. Only the internal energy control formulation has been implemented, and has only been allowed to optimize over a fraction of the iterations as the two-dimensional simulation. However, the cost function behavior shown in figure 35 is leveling-off as was observed in figure 9. Further iterations will determine if the three-dimensional optimization will follow the same behavior. The ability of mass or body-force controls to be any more successful than the current is yet to be seen.

6 Personnel supported during duration of grant

The work is being supervised by Prof. Freund at UIUC. Funding supported the PhD studies of Dr. Mingjun Wei, now a postdoc at Princeton University, and Mr. Randy Kleinman, a graduate student.

7 AFRL point of contact

Dr. Leonnard Shaw, last met at the AIAA Aeroacoustics Meeting, Monterey, CA, May, 2005.

8 Publications

1. J. B. FREUND & M. WEI, "Adjoint-based control of free shear flow noise," AIAA Paper 2003-3570 (2003).
2. M. WEI & J. B. FREUND, "Jet noise mechanism studied by optimal control," *Bull. of the Am. Physical Soc.*, **47**(10) (2003).

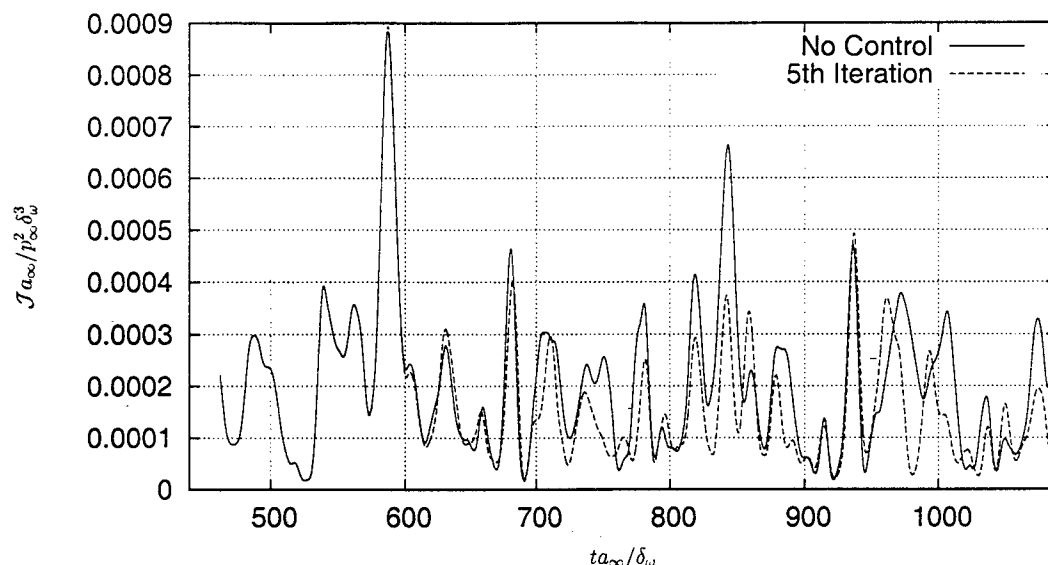


Figure 36: Plot of the cost function $\mathcal{J}(\phi)$ showing the cost on $y = -40$ with no control and after the fifth iteration.

3. J. B. FREUND & M. WEI, "An empirical 'lower bound' on free-shear-flow noise", *Mechanics of the 21st Century*, proceedings of the 21st International Congress on Theoretical and Applied Mechanics, Warsaw (2003).
4. J. B. FREUND, S. K. LELE & M. WEI, "The robustness of acoustic analogies," Proceedings of the 2004 Summer Program, Center For Turbulence Research (2004).
5. J. B. FREUND & M. WEI, "A quiet free shear flow," *Bull. of the Am. Physical Soc.*, **48**(10) (2004).
6. M. WEI, *Jet noise control by adjoint-based optimization*, PhD Thesis, Department of Theoretical and Applied Mechanics, University of Illinois at Urbana-Champaign (2005).
7. J. B. FREUND, A. SAMANTA, S. K. LELE & M. WEI, "The robustness of acoustic analogies," AIAA Paper 2005-2940 (2005).
8. J. B. FREUND & M. WEI, "Small changes that make a mixing layer very, very quiet," AIAA Paper 2005-0997 (2005).
9. M. WEI & J. B. FREUND, "A noise-controlled free shear flow," *J. Fluid Mech.*, **546**, 123-152 (2006).
10. A. SAMANTA, J. B. FREUND, M. WEI & S. K. LELE, "The robustness of acoustic analogies for predicting mixing-layer noise," submitted to *AIAA J.* (2006).
11. R. KLEINMAN & J. B. FREUND, "Adjoint-based control of the noise from a turbulent mixing layer," AIAA Paper 2006-2501 (2006).

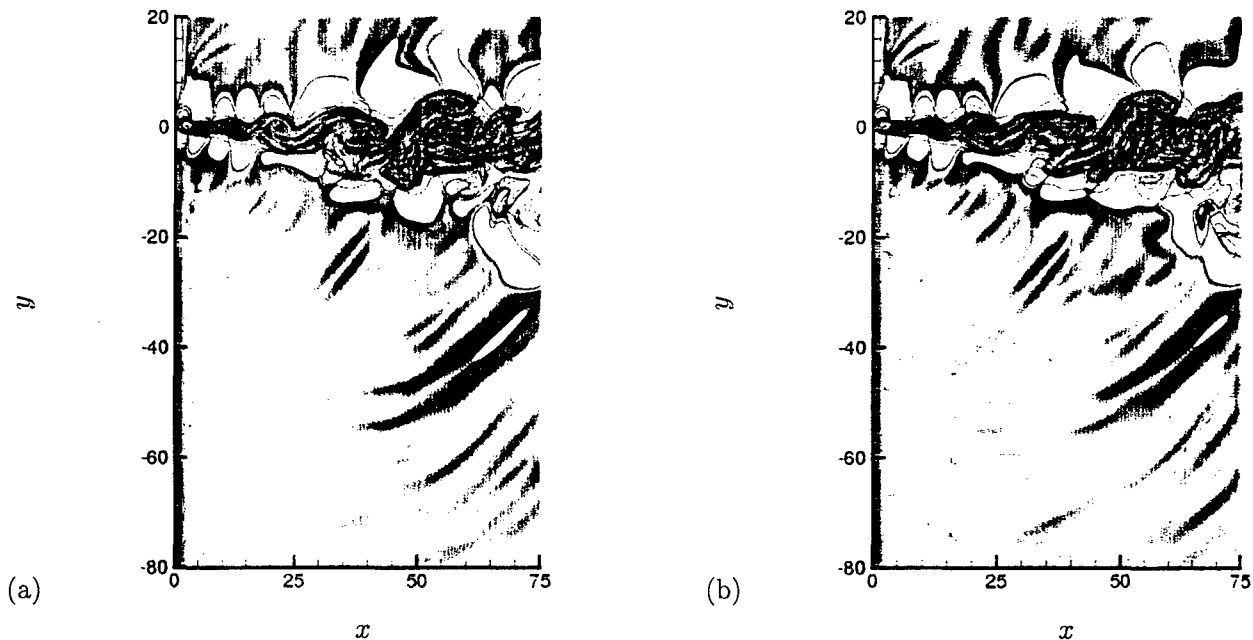


Figure 37: Comparison of the original dilatation and vorticity magnitude (a) and the field after the fifth iteration (b) at $ta_\infty/\delta_\omega = 831.38$. Contours of both quantities are the same for each plot.

9 Transitions

This effort is coordinated with ongoing efforts at United Technologies Research Center (UTRC) to model, simulate, predict, and reduce jet noise for Pratt & Whitney engines. Their experimental results showing the importance of the near-nozzle region at high Reynolds number motivated our focus on the near-nozzle region. Freund makes regular visits to UTRC to discuss jet noise and adjoint-based control of various types of turbulent jets. Our principal contact at UTRC is Satish Narayanan. The simulation databases are being made available to complement Prof. Samimy's efforts at OSU to control noise.

10 Acknowledgment/disclaimer

This work was sponsored by the Air Force Office of Scientific Research, USAF, under grant number F49620-03-1-0113. The views and conclusions contained herein are those of the authors and should not be interpreted as necessarily representing the official policies or endorsements, either expressed or implied, of the Air Force Office of Scientific Research or the U.S. Government.

A Compressible viscous flow equations

The compressible viscous flow equations were written in an operator form as

$$\mathcal{N}(\mathbf{q}) = [n_1(\mathbf{q}) \ n_2(\mathbf{q}) \ n_3(\mathbf{q}) \ n_4(\mathbf{q}) \ n_5(\mathbf{q})]^T = 0, \quad (54)$$

with

$$\begin{aligned}
n_1(\mathbf{q}) &= \frac{\partial \rho}{\partial t} + \frac{\partial \rho u_i}{\partial x_i} \\
n_{2,3,4}(\mathbf{q}) &= \frac{\partial \rho u_i}{\partial t} + \frac{\partial \rho u_i u_j}{\partial x_j} + \frac{\partial p}{\partial x_i} - \frac{\partial \tau_{ij}}{\partial x_j} \\
n_5(\mathbf{q}) &= \frac{\partial e}{\partial t} + \frac{\partial}{\partial x_j} [u_j(e + p)] - \frac{\gamma}{\text{Pr}(\gamma - 1)} \left[\frac{\partial^2}{\partial x_j^2} \left(\frac{p}{\rho} \right) \right] - \left[\frac{\partial}{\partial x_i} (\tau_{ij} u_j) \right],
\end{aligned} \tag{55}$$

where stresses

$$\tau_{ij} = \frac{1}{\text{Re}} \left[\left(\frac{\partial u_i}{\partial x_j} + \frac{\partial u_j}{\partial x_i} \right) - \frac{2}{3} \frac{\partial u_k}{\partial x_k} \delta_{ij} \right] \tag{56}$$

are for a Newtonian fluid with zero bulk viscosity, and the total energy e for our normalization is

$$e = \frac{p}{\gamma - 1} + \frac{1}{2} \rho u_i u_i, \tag{57}$$

including both internal and kinetic energy. Here, all variables were non-dimensionalized with ρ_∞ , a_∞ , δ_ω , and c_p , which gives a dimensionless gas constant $R = (\gamma - 1)/\gamma$, where γ is the ratio of the specific heats, and $\text{Re} = \rho_\infty a_\infty \delta_\omega / \mu$. For the two-dimensional equations, $n_4(\mathbf{q})$, u_3 , and $\frac{\partial}{\partial u_3}$ are identically zero.

B Two-dimensional Adjoint equations

Following the systematic procedure in section 4.3.3, the adjoint of the linearized perturbed two-dimensional compressible viscous flow equations is

$$\mathcal{N}^*(\mathbf{q})\mathbf{q}^* = \left(\mathbf{C}^* \frac{\partial}{\partial t} + \mathbf{A}^* \frac{\partial}{\partial x} + \mathbf{B}^* \frac{\partial}{\partial y} + \mathbf{D}^* \right) \mathbf{q}^*, \tag{58}$$

where

$$\mathbf{A}^* = \begin{bmatrix} u & u^2 & uv & \frac{1}{2}u(u^2 + v^2) \\ \rho & 2\rho u & \rho v & \frac{\gamma p}{\gamma - 1} + \frac{1}{2}\rho(3u^2 + v^2) + \frac{5}{3\text{Re}}\frac{\partial v}{\partial y} \\ 0 & 0 & \rho u & \rho uv - \frac{5}{3\text{Re}}\frac{\partial u}{\partial y} \\ 0 & \gamma - 1 & 0 & \gamma u \end{bmatrix}, \tag{59}$$

$$\mathbf{B}^* = \begin{bmatrix} v & uv & v^2 & \frac{1}{2}v(u^2 + v^2) \\ 0 & \rho v & 0 & \rho uv - \frac{5}{3\text{Re}}\frac{\partial v}{\partial x} \\ \rho & \rho u & 2\rho v & \frac{\gamma p}{\gamma - 1} + \frac{1}{2}\rho(u^2 + 3v^2) + \frac{5}{3\text{Re}}\frac{\partial u}{\partial x} \\ 0 & 0 & \gamma - 1 & \gamma v \end{bmatrix}, \tag{60}$$

$$\mathbf{C}^* = \begin{bmatrix} 1 & u & v & \frac{1}{2}(u^2 + v^2) \\ 0 & \rho & 0 & \rho u \\ 0 & 0 & \rho & \rho v \\ 0 & 0 & 0 & 1 \end{bmatrix}, \tag{61}$$

and

$$\mathbf{D}^* = \frac{1}{\text{Re}} \begin{bmatrix} 0 & 0 & 0 & -\frac{\gamma p}{\text{Pr}(\gamma - 1)} \rho^2 \left(\frac{\partial^2}{\partial x^2} + \frac{\partial^2}{\partial y^2} \right) \\ 0 & \frac{4}{3} \frac{\partial^2}{\partial x^2} + \frac{\partial^2}{\partial y^2} & \frac{1}{3} \frac{\partial^2}{\partial x \partial y} & \frac{4u}{3} \frac{\partial^2}{\partial x^2} + u \frac{\partial^2}{\partial y^2} + \frac{v}{3} \frac{\partial^2}{\partial x \partial y} \\ 0 & \frac{1}{3} \frac{\partial^2}{\partial x \partial y} & \frac{4}{3} \frac{\partial^2}{\partial y^2} + \frac{\partial^2}{\partial x^2} & \frac{4v}{3} \frac{\partial^2}{\partial y^2} + v \frac{\partial^2}{\partial x^2} + \frac{u}{3} \frac{\partial^2}{\partial x \partial y} \\ 0 & 0 & 0 & \frac{\gamma}{\text{Pr} \rho} \left(\frac{\partial^2}{\partial x^2} + \frac{\partial^2}{\partial y^2} \right) \end{bmatrix}. \tag{62}$$

These matrices all depend on the flow solutions, ρ , u , v , and w . In the numerical solution, \mathbf{C}^* was inverted every Runge-Kutta sub-step. The adjoint has a similar characteristics structure as the flow equations, which permits a one-dimensional characteristic boundary condition to be developed in a similar fashion.¹⁷

C Three-dimensional Adjoint equations

Following the systematic procedure in section 4.3.3, the adjoint of the linearized perturbed three-dimensional compressible viscous flow equations is

$$\mathcal{N}^*(\mathbf{q})\mathbf{q}^* = \left(\mathbf{C}^* \frac{\partial}{\partial t} + \mathbf{A}^* \frac{\partial}{\partial x} + \mathbf{B}^* \frac{\partial}{\partial y} + \mathbf{E}^* \frac{\partial}{\partial z} + \mathbf{D}^* \right) \mathbf{q}^* = 0 \quad (63)$$

$$\mathbf{C}^* = \begin{bmatrix} 1 & u & v & w & \frac{1}{2}(u^2 + v^2 + w^2) \\ 0 & \rho & 0 & 0 & \rho u \\ 0 & 0 & \rho & 0 & \rho v \\ 0 & 0 & 0 & \rho & \rho w \\ 0 & 0 & 0 & 0 & \frac{1}{\gamma-1} \end{bmatrix}$$

$$\mathbf{A}^* = \begin{bmatrix} u & u^2 & uv & uw & \frac{1}{2}u(u^2 + v^2 + w^2) \\ \rho & 2\rho u & \rho v & \rho w & \frac{\gamma p}{(\gamma-1)} + \frac{\rho}{2}(3u^2 + v^2 + w^2) + \frac{5}{3\text{Re}}\left(\frac{\partial v}{\partial y} + \frac{\partial w}{\partial z}\right) \\ 0 & 0 & \rho u & 0 & \rho uv - \frac{5}{3\text{Re}}\frac{\partial u}{\partial y} \\ 0 & 0 & 0 & \rho u & \rho uw - \frac{5}{3\text{Re}}\frac{\partial u}{\partial z} \\ 0 & 1 & 0 & 0 & \frac{\gamma u}{\gamma-1} \end{bmatrix}$$

$$\mathbf{B}^* = \begin{bmatrix} v & uv & v^2 & vw & \frac{1}{2}v(u^2 + v^2 + w^2) \\ 0 & \rho v & 0 & 0 & \rho uv - \frac{5}{3\text{Re}}\frac{\partial v}{\partial x} \\ \rho & \rho u & 2\rho v & \rho w & \frac{\gamma p}{(\gamma-1)} + \frac{\rho}{2}(u^2 + 3v^2 + w^2) + \frac{5}{3\text{Re}}\left(\frac{\partial u}{\partial x} + \frac{\partial w}{\partial z}\right) \\ 0 & 0 & 0 & \rho v & \rho vw - \frac{5}{3\text{Re}}\frac{\partial v}{\partial z} \\ 0 & 0 & 1 & 0 & \frac{\gamma v}{\gamma-1} \end{bmatrix}$$

$$\mathbf{E}^* = \begin{bmatrix} w & uw & vw & w^2 & \frac{1}{2}w(u^2 + v^2 + w^2) \\ 0 & \rho w & 0 & 0 & \rho uw - \frac{5}{3\text{Re}}\frac{\partial w}{\partial x} \\ 0 & 0 & \rho w & 0 & \rho vw - \frac{5}{3\text{Re}}\frac{\partial w}{\partial y} \\ \rho & \rho u & \rho v & 2\rho w & \frac{\gamma p}{(\gamma-1)} + \frac{\rho}{2}(u^2 + v^2 + 3w^2) + \frac{5}{3\text{Re}}\left(\frac{\partial u}{\partial x} + \frac{\partial v}{\partial y}\right) \\ 0 & 0 & 0 & 1 & \frac{\gamma w}{\gamma-1} \end{bmatrix}$$

$$\mathbf{D}^* = \frac{1}{\text{Re}} \begin{bmatrix} 0 & 0 & 0 & 0 & -\frac{\gamma p}{\text{Pr}(\gamma-1)\rho^2} \left(\frac{\partial^2}{\partial x^2} + \frac{\partial^2}{\partial y^2} + \frac{\partial^2}{\partial z^2} \right) \\ 0 & \frac{4}{3}\frac{\partial^2}{\partial x^2} + \frac{\partial^2}{\partial y^2} + \frac{\partial^2}{\partial z^2} & \frac{1}{3}\frac{\partial^2}{\partial x \partial y} & \frac{1}{3}\frac{\partial^2}{\partial x \partial z} & \frac{4u}{3}\frac{\partial^2}{\partial x^2} + u \left(\frac{\partial^2}{\partial y^2} + \frac{\partial^2}{\partial z^2} \right) + \frac{u}{3}\frac{\partial^2}{\partial x \partial y} + \frac{uw}{3}\frac{\partial^2}{\partial x \partial z} \\ 0 & \frac{1}{3}\frac{\partial^2}{\partial x \partial y} & \frac{\partial^2}{\partial x^2} + \frac{4}{3}\frac{\partial^2}{\partial y^2} + \frac{\partial^2}{\partial z^2} & \frac{1}{3}\frac{\partial^2}{\partial y \partial z} & \frac{4v}{3}\frac{\partial^2}{\partial y^2} + v \left(\frac{\partial^2}{\partial x^2} + \frac{\partial^2}{\partial z^2} \right) + \frac{v}{3}\frac{\partial^2}{\partial x \partial y} + \frac{vw}{3}\frac{\partial^2}{\partial y \partial z} \\ 0 & \frac{1}{3}\frac{\partial^2}{\partial x \partial z} & \frac{1}{3}\frac{\partial^2}{\partial y \partial z} & \frac{\partial^2}{\partial x^2} + \frac{\partial^2}{\partial y^2} + \frac{4}{3}\frac{\partial^2}{\partial z^2} & \frac{4w}{3}\frac{\partial^2}{\partial z^2} + w \left(\frac{\partial^2}{\partial x^2} + \frac{\partial^2}{\partial y^2} \right) + \frac{w}{3}\frac{\partial^2}{\partial x \partial z} + \frac{w}{3}\frac{\partial^2}{\partial y \partial z} \\ 0 & 0 & 0 & 0 & \frac{\gamma}{\text{Pr}(\gamma-1)\rho} \left(\frac{\partial^2}{\partial x^2} + \frac{\partial^2}{\partial y^2} + \frac{\partial^2}{\partial z^2} \right) \end{bmatrix}$$

These equations were solved in a similar manner as that mentioned in Appendix B.

References

- [1] G. McKinney, Air Force Office of Scientific Research Publication: Research Highlights, Sept./Oct 1998 (also <http://ecs.rams.com/afosr/af/af/any/text/any/afrrhoct.htm>).
- [2] M. Samimy, personal communication.
- [3] J. B. Freund, "Noise sources in a low-Reynolds-number turbulent jet at Mach 0.9," *J. Fluid Mech.* **438**, 277 (2001).
- [4] T. R. Bewley, P. Moin and R. Temam, "Dns-based predictive control of turbulence: an optimal benchmark target for feedback algorithms," *J. Fluid Mech.* **447**, 179 (2001).
- [5] G. M. Lilley, "Jet noise: Classical theory and experiments," In *Aeroacoustics of Flight Vehicles* edited by H. Hubbard. NASA RP 1258 (1991).
- [6] "Separate flow low noise nozzle project," Nasa Aerospace Technology News, Volume 1, Issue 2 (September 2000).
- [7] M. J. Lighthill, "On sound generated aerodynamically: I. General theory," *Proc. Royal Soc. Lond. A* **211**, 564 (1952).
- [8] P. Huerre and D. G. Crighton, "Sound generation by instability waves in a low Mach number jet," AIAA paper 83-0661 (1983).
- [9] J. E. Ffowcs Williams and A. J. Kempton, "The noise from the large-scale structure of a jet," *J. Fluid Mech.* **84**, 673 (1978).
- [10] D. G. Crighton and P. Huerre, "Shear-layer pressure fluctuations and superdirective acoustic sources," *J. Fluid Mech.* **220**, 255 (1990).
- [11] J. T. C. Liu, "Developing large-scale wavelike eddies and the near jet noise field," *J. Fluid Mech.* **62**, 437 (1974).
- [12] R. Mankbadi and J. T. C. Liu, "Sound generated aerodynamically revisited: large-scale structures in a turbulent jet as a source of sound," *Phil. Trans. R. Soc. Lond. A* **311**, 183 (1984).
- [13] S. C. Crow, "Acoustic gain of a turbulent jet," *Bull. Am. Phys. Soc. Paper IE*. 6. (1972).
- [14] S. K. Lele, "Noise radiation from wave-packet models of large-scale jet turbulence," *Bull. Am. Phys. Soc.*, **48**(10) Paper EG. 2. (2003).
- [15] J. B. Freund, "Acoustic sources in a turbulent jet: a direct numerical simulation study," AIAA Paper 99-1858 (1999).
- [16] T. Colonius, S. K. Lele and P. Moin, "Sound generation in a mixing layer," *J. Fluid Mech.* **330**, 375 (1997).
- [17] M. Wei, *Jet Noise Control by Adjoint-based Optimization*, Ph.D. thesis, Department of Theoretical and Applied Mechanics, University of Illinois at Urbana-Champaign, Urbana, Illinois (2004).

- [18] M. E. Goldstein, "A generalized acoustic analogy," *J. Fluid Mech.* **488**, 315 (2003).
- [19] J. E. Ffowcs Williams. "The noise from turbulence convected at high speed," *Phil. Trans. Roy. Soc. A* **255**, 469 (1963).
- [20] D. G. Crighton, "Basic principles of aerodynamic noise generation," *Progress in Aerospace Sciences* **16**, 31 (1975).
- [21] S. K. Lele, "Compact finite difference schemes with spectral-like resolution," *J. Comp. Phys.* **103**, 16 (1992).
- [22] C. K. W. Tam and J. C. Webb, "Dispersion-relation-preserving finite difference schemes for computational acoustics," *J. Comp. Phys.* **107**, 262 (Aug 1993).
- [23] J. B. Freund, "A proposed inflow/outflow boundary condition for direct computation of aerodynamic sound," *AIAA J.* **35**, 740 (1997).
- [24] P. A. Monkewitz and P. Huerre, "Influence of the velocity ratio on the spatial instability of mixing layers," *Phys. Fluids* **25**, 1137 (1988).
- [25] N. Sandham and W. Reynolds, "Three-dimensional simulations of large eddies in the compressible mixing layer," *J. Fluid Mech.* **224**, 133 (1991).
- [26] W. H. Press, B. P. Flannery, S. A. Teukolsky and W. T. Vetterling, *Numerical Recipes* (Cambridge) (1986).
- [27] J. Bridges and G. G. Podboy, "Measurements of two-point velocity correlations in a round jet with application to jet noise," AIAA paper 99-1966 (1999).
- [28] B. E. Mitchell, S. K. Lele and P. Moin, "Direct computation of the sound generated by vortex pairing in an axisymmetric jet," *J. Fluid Mech.* **383**, 113 (1999).
- [29] P. Holmes, J. L. Lumley and G. Berkooz, *Turbulence, Coherent Structures, Dynamical Systems and Symmetry* (Cambridge University Press, Cambridge) (1996).
- [30] L. Sirovich, "Chaotic dynamics of coherent structures. Parts I-III," *Quarterly of Applied Math.* **XLV**, 561 (1987).
- [31] J. Laufer and T.-C. Yen, "Noise generation by a low-mach-number jet," *J. Fluid Mech.* **134**, 1 (1983).
- [32] J. B. Freund, "Decomposition of the lighthill noise source," submitted to *Phys. Fluids* (2002).
- [33] R. E. A. Arndt, D. F. Long and M. N. Glauser, "The proper orthogonal decomposition of pressure fluctuations surrounding a turbulent jet," *J. Fluid Mech.* **340**, 1 (1997).
- [34] J. B. Freund and T. G. Fleischman, "Ray traces through unsteady jet turbulence," *Int. J. Aeroacoustics* **1**, 83 (2002).
- [35] J. Kastner, M. Samimy, J. Hileman and J. B. Freund, "Comparison of noise sources in high and low reynolds number high speed jets," AIAA Paper submitted Aeroacoustics Meeting (2005).

- [36] R. Hixon, V. Allampalli, N. Nallasamy and S. Sawyer, "High-accuracy large-step explicit runge-kutta (hale-rk) schemes for computational aeroacoustics," 44th Aerospace Sciences Meeting and Exhibit, Reno, AIAA Paper 2006-0797 (2006).
- [37] C. Lui and S. K. Lele, "Direct numerical simulation of spatially developing, compressible, turbulent mixing layers," AIAA Paper 2001-0291 (2001).